Are All Single Atoms Created Equal? *Surface Density Dependent Catalytic Activity of Single Pd Atoms Supported on Ceria*

Yongseon Kim[1,||], Greg Collinge[2,3,||], Mal-Soon Lee[2,3], Konstantin Khivantsev[3], Sung June Cho[4,*], Vassiliki-Alexandra Glezakou[2,3], Roger Rousseau[2,3,*], Janos Szanyi[3,*], Ja Hun Kwak[1,*]

[1] Department of Chemical Engineering, Ulsan National Institute of Science and Technology (UNIST), 50 UNIST-gil, Ulsan 44919, Republic of Korea

[2] Physical and Computational Sciences Directorate and Institute for Integrated Catalysis, Pacific Northwest National Laboratory, Richland, WA 99354, USA

[3] Institute for Integrated Catalysis, Pacific Northwest National Laboratory, Richland, WA 99352 USA

[4] Department of Chemical Engineering, Chonnam National University, 77 Yongbong-ro, Buk-gu, Gwangju 61186, Republic of Korea

[*]*Corresponding authors:* sjcho@jnu.ac.kr, roger.rousseau@pnnl.gov, janos.szanyi@pnnl.gov, jhkwak@unist.ac.kr

[||] These authors contributed equally.

ABSTRACT

The analogy between single atom catalysts (SACs) and molecular catalysts predicts that the specific catalytic activity of these systems is constant. We provide evidence that this prediction is not necessarily true. As a case in point, we show that the specific activity over ceria-supported single Pd atoms linearly increases with metal atom density, originating from the cumulative enhancement of lattice oxygen mobility. The long-range electrostatic fingerprints (~1.5 nm) around each Pd site overlap with each other as surface Pd density increases, resulting in the observed deviation from constant specific activity. These cooperative effects exhaust previously active O atoms above a certain Pd density, leading to their permanent removal and consequent drop in reaction rate. The findings of our combined experimental and computational study show that the specific catalytic activity of reducible oxide-supported single atom catalysts can be tuned by varying the surface density of single metal atoms.

MAIN

Supported single atom catalysts (SACs) have attracted considerable attention owing to their unique activity, efficient utilization of supported noble metals, and potentially bridging the gap between homogeneous and heterogeneous catalysis.[1-4] Increasing the surface metal density of SACs is commonly sought after to increase the mass activity of industrial catalysts.[5-10] However, such efforts assume that the active sites of SACs exhibit constant specific activity.[1,11-13] Here, using CO oxidation as a probe reaction, we show that, the specific activity of Pd/CeO_2 SACs increases with Pd density due to synergistic nonlocal effects. This phenomenon, however, is support-dependent as Pd SACs supported on non-reducible γ-Al_2O_3 exhibit constant specific activity for CO oxidation.

Numerous SACs have been characterized and reported to exhibit high activity for the CO oxidation reaction including the seminal Pt/FeO_x catalyst.[14] The charge state of the single atom centers is commonly invoked to explain this activity,[15] reportedly enhancing CO and/or O_2 adsorption. Subsequently, the choice of support and its redox state has been shown to impact CO oxidation activity greatly,[16,17] with irreducible supports, such as γ-Al_2O_3 or MgO, identified as comparatively inactive[18] or unstable[19-21] without modification such as the induction of defect sites[22] or the addition of La[23] or other heteroatom substituents.[24] Conversely, single atoms on reducible supports show considerable CO oxidation activity.[25-27] Some supports have even been reported to allow the stabilization of metallic single atoms.[28] Spezzati et al. reported high CO-oxidation activity of isolated Pd atoms supported on CeO_2(111) and identified a PdO_x species as the active site.[29,30] However, despite considerable research efforts on SACs, the effect of surface density of single metal atoms on catalytic activity has not been elucidated.

In this study, we report the synergistic effect between single Pd atoms supported on CeO_2. H_2-temperatrue programmed reduction (TPR) and in-situ Raman studies employed in this work clearly show that the reducibility of the support is enhanced as the density of single Pd atoms increases. Density functional theory (DFT) calculations confirm the lowering in oxygen vacancy formation energies as the surface Pd density increases, while CO and O_2 adsorption

energies remain unaffected. This suggests that the observed specific activity trends are due to the activation of lattice O by Pd. Charge and spin density analysis allow us to identify the active site as an overoxidized $Pd^{>2+}$ in a $[PdO_4]$ square planar complex consistent with X-ray Adsorption Spectroscopy (XAS). The Pd atom is overoxidized, past +2, and its coordinating oxygens are valence unsaturated, making $[PdO_4]$ an excellent oxidizer with a considerable— and importantly, cumulative, range of effect. Thus, as the surface density of $[PdO_4]$ complexes increases, their individual oxidation power also increases. The support mediates this process, allowing for the shuttling of excess charge to nearby $[PdO_4]$, explaining why γ-Al_2O_3, a non-reducible support, does not exhibit the same synergy.

RESULTS

CO oxidation on Pd/CeO$_2$

The effect of surface single atom density on the catalytic properties of Pd/CeO_2 (see Figure S1 – S3 for characterization of CeO_2) and Pd/Al_2O_3 catalysts was investigated in the model reaction of CO oxidation as a function of surface Pd density, displayed in Figure 1(a) (Figure S4(a) shows the relationship as a function of Pd weight loading).
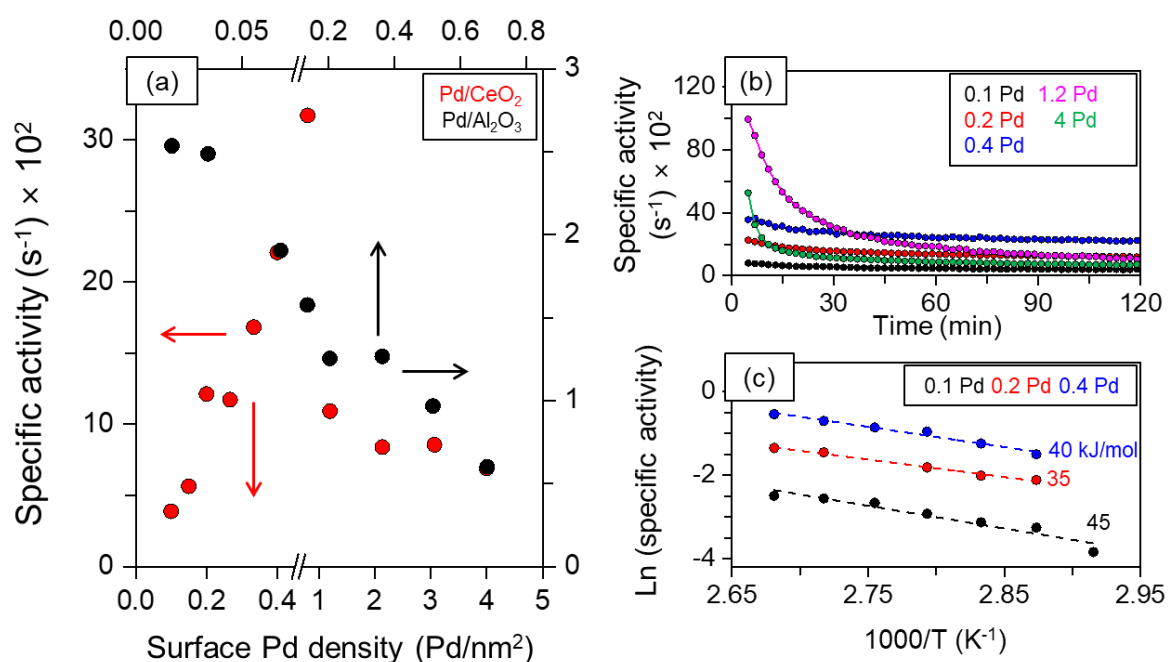
Figure 1. (a) Specific activity of CO oxidation at steady state as a function of surface Pd density of Pd/CeO_2 and Pd/Al_2O_3. (b) Specific activity of Pd/CeO_2 as function of time. (c) Arrhenius plots of 0.1, 0.2 and 0.4 Pd/CeO_2 catalysts for CO oxidation.

The specific activity of Pd/CeO_2 catalysts increased linearly with surface Pd density up to ~0.8 Pd/nm^2. This behavior was observed for both initial (Figure S4(b)) and steady state activities (Figure 1(a)). In the contrasting case of Pd/Al_2O_3 catalysts, the specific activity was constant below ~0.034 Pd /nm^2, in agreement with previously reported results.[1,11,12] Specific activity as a function of time for a selected series of Pd/CeO_2 catalysts is also shown in Figure 1(b), (for the entire series of Pd/CeO_2 and Pd/Al_2O_3 catalysts, see Figure S4(c) and (d)). Pd/CeO_2 catalysts with Pd surface densities in the range of 0.1-0.8 Pd /nm^2 deactivated slowly while catalysts with surface densities between 1.2-4 Pd/nm^2 underwent rapid deactivation. Sintering of Pd atoms/small metal clusters and, as we will show, the permanent removal of previously catalytically active lattice O atoms are primarily responsible for this activity loss. The apparent activation energies for Pd/CeO_2 catalysts with Pd surface densities of 0.1, 0.2 and 0.4 Pd/nm^2, estimated from Arrhenius plots in Figure 1(c), were 45, 35 and 40 kJ/mol, respectively. These values are consistent with a Mars-van Krevelen (MvK) mechanism.[31-35]

Aberration-corrected high angle annular dark field scanning transmission microscopy (AC-HAADF-STEM) imaging was used to visualize Pd atoms/particles in the CeO_2 and Al_2O_3-supported catalysts (Figures S5 and S6). Due to low z-contrast between Pd (z = 46) and Ce (z = 58), we could not observe single Pd atoms in Pd/CeO_2 samples with Pd loading ≤0.8 Pd/nm^2.[36-38] On 4 Pd/CeO_2, Pd nanoparticles were observed despite the poor contrast, implying their absence in the lower Pd density sample. For 0.034 Pd/Al_2O_3, despite the higher z-contrast between Pd and Al, no Pd nanoparticles were observed, indicating that Pd is atomically dispersed. At higher Pd surface densities (e.g., 0.20 Pd/Al_2O_3) distinctive Pd nanoparticles were observed.

Since we could not directly confirm the presence of atomically dispersed Pd on CeO_2, additional structural analysis was carried out. Pd K-edge X-ray Adsorption Near Edge Spectra

(XANES) (Figure S7) and extended x-ray absorption fine structure (EXAFS) data (Figure S8) were further used to estimate structural parameters (Table 1). The Fourier transformed EXAFS spectra show primarily a Pd-O scattering at 1.99 Å with coordination number of 3.8±0.6 and 3.7±0.5 for 0.8 and 4 Pd/CeO$_2$, respectively. In bulk PdO, Pd-Pd scattering appears around 3.06 and 3.45 Å with 4 and 8 coordination number, respectively.[39] However, no Pd-Pd bond was observed in either 0.8 or 4 Pd/CeO$_2$ samples. Interestingly, the corresponding XANES is shifted relative to that of PdO, indicating Pd to be in an oxidation state greater than 2+. These results suggest that Pd is highly dispersed with Pd-O coordination number around 4 in an overoxidized charge state.

Table 1. Structural parameters from Pd K-edge EXAFS analysis for 0.8 and 4 Pd/CeO$_2$.[a]

Sample	Pair	CN[b]	Bond distance (Å)	σ^2(pm^2)[c]	ΔE(eV)[d]	R-factor (%)
0.8 Pd/CeO$_2$	Pd-O	3.8±0.6	1.99±0.02	52±11	4.9±2.5	3.0
4 Pd/CeO$_2$	Pd-O	3.7±0.5	1.99±0.01	11±18	4.3±102	1.3

(a)　Many-body reduction factor, S02 was set to 0.86. The number of the free fitting parameter for XAFS data, 11 was always less than the number of independent points given by the Nyquist theorem.
(b)　Coordination number, (c) The Debye-Waller factor and (d) Energy shift

CeO$_2$ Redox Properties Modified by Pd Loading
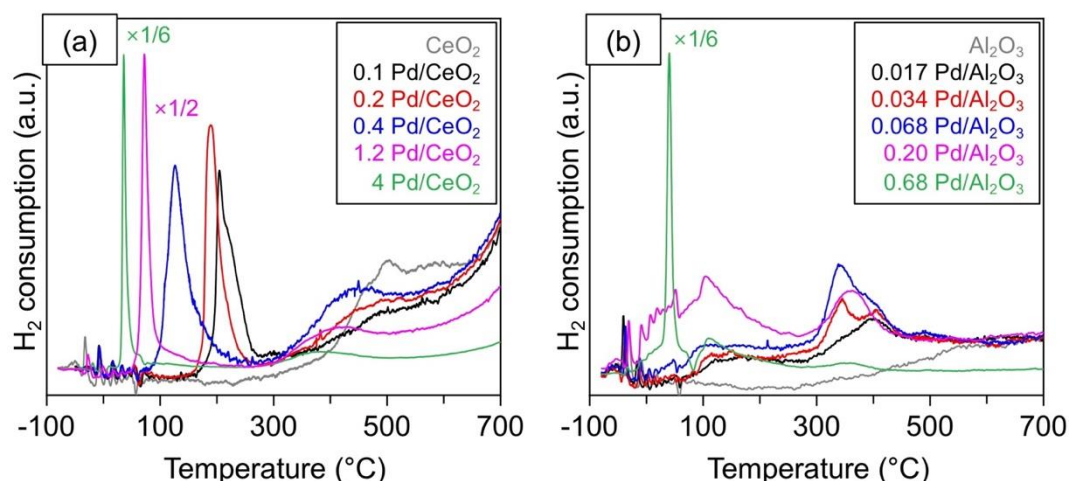
Figure 2. H$_2$-TPR profiles of (a) Pd/CeO$_2$ (m$_{cat}$ = 0.05 g) and (b) Pd/Al$_2$O$_3$ (m$_{cat}$ = 0.1 g). The same scale of y-axis is used for the figures.

Since CeO$_2$-based CO oxidation catalysts follow the MvK mechanism,[35,40-44] the activity must be related with the redox properties of catalysts. To gain information about this, we conducted H$_2$-TPR, see Figure 2(a) and (b) for Pd/CeO$_2$ and Pd/Al$_2$O$_3$ catalysts, respectively.

On bare CeO_2, surface and bulk reduction peaks at 510°C and above 700°C were observed, respectively.[40] With Pd present, the TPR profile dramatically changed. The intensity of the reduction peak at 510 °C decreased and a new reduction peak appeared at 205 °C for 0.1 Pd/CeO_2. The reduction peak gradually shifted toward lower temperature with increasing Pd surface density, appearing at 125 °C for 0.4 Pd/CeO_2.[45-47] At even higher surface Pd density, very sharp and intense reduction peaks arose under 100 °C.

Table 2. Summary of H_2-TPR over Pd/CeO_2

Catalyst	Pd content ($\mu mol_{Pd}/g_{cat}$)	Surface Pd density (Pd/nm^2)	H_2-TPR (< 300 °C)			Specific activity ×10^2 [(b)]
			Reduction temperature (°C)	H_2 consumption ($\mu mol/g_{cat}$)	CeO_2 reduction ($\mu mol/g_{cat}$) [(a)]	
0.1 Pd/CeO_2	2.4	0.1	205	56.2	53.9	3.9
0.2 Pd/CeO_2	4.7	0.2	192	64.5	59.8	12.1
0.4 Pd/CeO_2	9.4	0.4	129	77.5	68.1	22.1
1.2 Pd/CeO_2	28.3	1.2	73	92.1	63.8	10.9
4 Pd/CeO_2	94.3	4.1	36	125.6	31.3	6.9

(a) CeO_2 reduction ($\mu mol/g_{cat}$) = H_2 consumption – Pd content
(b) Specific activity (s^{-1}) at steady state

H_2-TPR clearly reveals that the hydrogen consumption (see Table 2) far exceeded the amount of Pd loaded. We calculated the contribution from CeO_2 reduction by subtracting off the H_2 needed for Pd reduction. Reduction increased with surface Pd density at atomic Pd dispersion (0.1-0.4 Pd/nm^2) and follows a linear trend just like the specific activity (Figure S9). This result suggests a causal relationship between enhanced reducibility of CeO_2 and increase in specific activity, ultimately derived from higher surface Pd density. As the Pd loading is further increased past 0.4 Pd/nm^2, CeO_2 reduction decreased and correspondingly, so did specific activity. This could be due to a decrease in Pd dispersion, but may also be due to lattice oxygen deactivation, which we will return to shortly. As seen in Figure 2(b), the reduction temperature of Pd/Al_2O_3 catalysts was not affected by the surface Pd density. Very small amounts of H_2 were consumed at low-temperature (< 50 °C) on 0.017-0.20 Pd/Al_2O_3 and a strong reduction peak is observed only with 0.68 Pd/Al_2O_3, well beyond the point at which nanoparticles form.[48, 49]
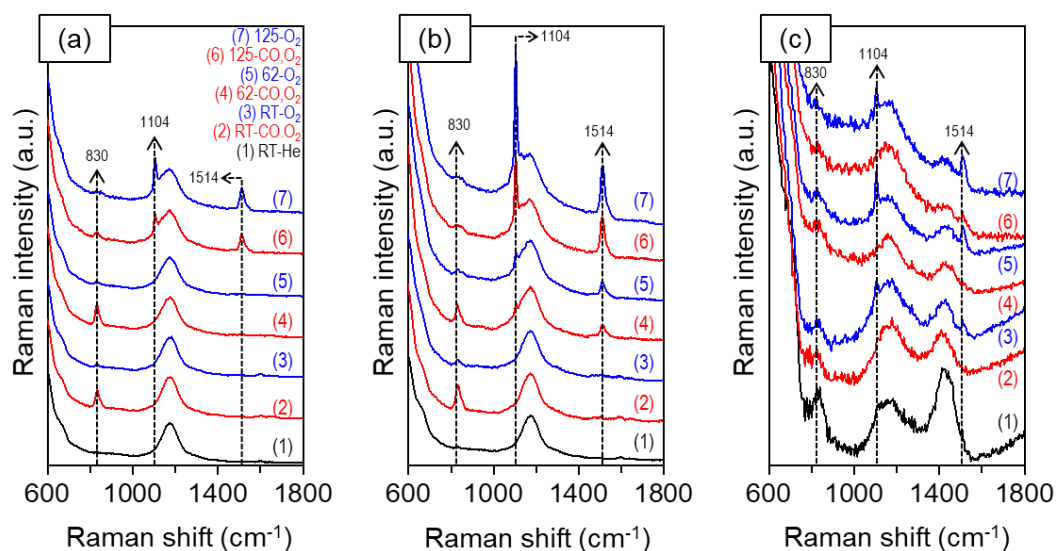
Figure 3. in-situ Raman spectra of (a) 0.2 Pd/CeO$_2$, (b) 0.4 Pd/CeO$_2$ and (c) 4 Pd/CeO$_2$ ((1) room temperature (RT) – He, (2) RT – 1%CO+2.5%O$_2$/He, (3) RT – 2.5%O$_2$/He, (4) 62 °C – 1%CO+2.5%O$_2$/He, (5) 62 °C – 2.5%O$_2$/He, (6) 125 °C – 1%CO+2.5%O$_2$/He, and (7) 125 °C – 2.5%O$_2$/He). Raman intensity was normalized with F$_{2g}$ (450-470 cm^{-1}) band. The same scale of y-axis is used for the figures.

To investigate the observed CeO$_2$ reduction under reaction conditions, we performed in-situ Raman spectroscopy on the 0.2, 0.4 and 4 Pd/CeO$_2$ catalysts at room temperature (RT), 62°C, and 125°C. The results obtained are displayed in Figure 3. All samples were pretreated at 350°C in 20% O$_2$/He for 0.5 h. At RT under He only, a Raman band representative of CeO$_2$ at 450-470 cm^{-1} was observed along with weak bands at 270, 600 and 1174 cm^{-1} (Figure S10).[40,50,51] In CO+O$_2$, a distinct band at 830 cm^{-1} was observed for 0.2 and 0.4 Pd/CeO$_2$ catalysts. On the 4 Pd/CeO$_2$ catalyst, this Raman band was rather intense after pre-treatment and He flushing, but this band decreased in the presence of CO+O$_2$ at room temperature. The 830 cm^{-1} band has been attributed to adsorbed peroxide species (O$_2^{2-}$) on isolated two-electron defect sites, indicating oxygen vacancy is formed on Pd/CeO$_2$ under reaction condition.[50] As CO is removed from the gas stream, the characteristic Raman band for the peroxide disappeared on both single atom-containing catalysts (0.2 and 0.4 Pd/CeO$_2$). At 62 °C, the Raman band of peroxide species re-appeared in the CO+O$_2$ stream. The most noticeable feature is the development of new bands at 1104 and 1514 cm^{-1} for the 0.4 Pd/CeO$_2$. These bands are assigned to superoxide (O$_2^-$) and weakly bound dioxygen (O$_2^{\delta-}$) species, respectively.[52] According to Hess et al.,[52] those two dioxygen species can be attributed to the

creation of oxygen vacancies during CO oxidation and transfer of electron to adsorbed oxygen molecule. As the temperature was further increased to 125 °C, the peroxide peak (830 cm^{-1}) appeared in a weak intensity under CO+O_2 flow. Features for superoxide (1104 cm^{-1}) and weakly bound dioxygen (1514 cm^{-1}) appeared on 0.2 Pd/CeO_2, but their intensities were much lower than in the 0.4 Pd/CeO_2 catalyst. When CO was taken out of the gas stream, the two features became very prominent on both 0.2 and 0.4 Pd/CeO_2 catalysts, which might be due to reaction of the charged oxygen species (O_2^- or $O_2^{\delta-}$) with gas phase CO or removal of adsorbed CO on oxygen vacancies. On the other hand, as the surface Pd density further increased to 4, the intensity of the dioxygen species became significantly lower than over 0.4 Pd/CeO_2. The comparison of Raman spectra of 0.2 and 0.4 Pd/CeO_2 catalysts clearly shows the facile formation of oxygen vacancies on CeO_2 surface with higher surface density of single Pd atoms in reaction conditions. This result manifests itself in improved oxygen vacancy formation with surface density of atomic Pd, consistent with results from H_2-TPR.

In situ transmission FTIR spectroscopy was used to monitor both the nature of Pd species present on the CeO_2 support after oxidation at 623 K and the variation of the reducibility of CeO_2 as a function of Pd loading using CO as a probe molecule. The IR spectra collected during sequential CO adsorption over Pd/CeO_2 catalysts with Pd loadings of 0.2, 0.4 and 4 Pd/nm^2 are displayed in Figure S11. IR bands characteristic of Pd ions are observed exclusively for the 0.2 Pd/CeO_2 sample with characteristic IR features centered between 2098 and 2154 cm^{-1}. The 0.4 Pd/CeO_2 catalyst exhibits similar IR features of adsorbed CO, however, the intensity ratio of the high and low frequency bands changes dramatically as the Pd loading increases, indicating changes in the population of Pd ions in different environments on(in) the CeO_2 surface. The series of IR spectra collected from the 4 Pd/CeO_2 sample is fundamentally different from the those of the other two catalysts: they are dominated by IR features of CO adsorbed on metallic Pd sites (Pd particles). IR bands at 2082-2098 and at 1917-1952 cm^{-1} represent CO molecules bound linearly and in a bridging configuration to Pd^0 centers of metal particles, respectively. It is very interesting to note that upon CO introduction onto all three samples the formation of CO_2 is clearly observed. However, while CO_2 is present as an

adsorbed species (sharp IR band at 2351 cm^{-1}) on the atomically dispersed Pd/CeO$_2$ samples, we only observe the formation of gas phase CO$_2$ (2349 cm^{-1}) over the Pd particles. We propose that the origin of CO$_2$ formed over the single atom-containing samples is fundamentally different from that formed on supported Pd particles. The results of DFT calculations, which will be discussed below, clearly demonstrate that the presence of single Pd atoms significantly reduces the energy of oxygen vacancy formation on CeO$_2$. This, in turn, means that certain oxygen species on the CeO$_2$ surface in the vicinity of single Pd atoms become very reactive toward CO, and readily produce CO$_2$. Since these experiments are carried out at room temperature the thus-formed CO$_2$ stays on the CeO$_2$ surface interacting with the oxygen vacancies. In contrast, when Pd particles are present on the CeO$_2$ support, CO$_2$ is formed by the reaction of CO with the surface oxide layer formed on the Pd particles during the 673 K oxidation prior to CO adsorption.

Calculated Properties of the Pd/CeO$_2$ System

Density functional theory calculations, on the dominant oxygen-terminated CeO$_2$(100), were employed to provide molecular level insights into the effect of surface Pd density on CO oxidation activity. The 4-fold hollow sites of this surface can stabilize Pd adatoms. However, as shown in Figure S12, upon deposition of single Pd atoms, exposing the stoichiometric CeO$_2$(100) surface to any partial pressure of oxygen will result in the irreversible adsorption of one additional O$_2$ molecule per Pd atom to form (PdO$_2$)$_1$ single-metal-centers, see Figure S12a. These (PdO$_2$)$_1$ reside in a square planar configuration, with a 4-fold Pd coordination to surface-bound oxygen atoms, labeled O1 – O4 in Figure 4a, Pd-O bond lengths of 1.94 Å – 1.98 Å. This is in excellent agreement with the EXAFS results shown in Table 1 (CN of 3.8 and Pd-O bond length of 1.99 Å). Increasing the surface Pd density therefore corresponds to decreasing the spatial separation of these [PdO$_4$] sites.
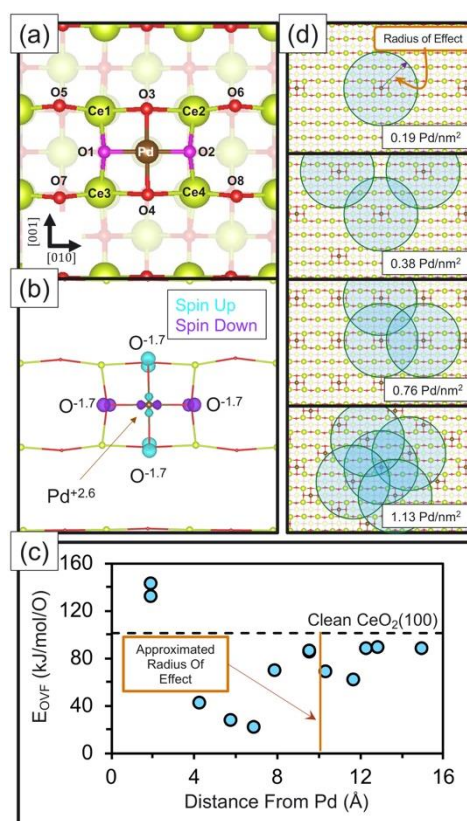
Figure 4. (a) Top-down view of the square planar [PdO$_4$] active site on the CeO$_2$(100) surface with atoms nearby Pd labeled to aid discussion found in the SI. (b) Spin density plot of the [PdO$_4$] active site. (c) Oxygen vacancy formation energies (E$_{OVF}$) as a function of distance from Pd. (d) Approximate zone(s) of effect (semi-transparent blue circles) of each [PdO$_4$], illustrating how overlapping zones produce a cumulative effect as Pd surface density increases. Brown atoms are Pd, green and red atoms are Ce and O of the CeO$_2$(100) surface, respectively, and the two magenta atoms are O adatoms.

Through Bader analysis of the electron and spin density around each atom in and surrounding the [PdO$_4$] complex (see the SI for details), we are able to determine their electronic states. We find that Pd is in an unusually overoxidized ~2.6+ state (consistent with our XANES results) with its surrounding O atoms in markedly unsaturated charge states of ~1.7-. The incomplete valence saturation of Pd 4d and O 2p orbitals can be seen in Figure 4b, clearly showing the presence of spin density (i.e., unpaired charge) in these orbitals, indicative of partially charged states. This overoxidation occurs because the two additional O atoms (O1 and O2 in Figure 4a) require four total electrons to reach valence saturation, while neither Pd nor the Ce^{4+} of the surface can be oxidized sufficiently to provide all four of these electrons. Instead, Pd provides ~2.6 electrons (apparently the limit of its reducing power) and the remaining electron deficiency is shared equally amongst the 4 Pd-coordinated O atoms (O1 – O4 in Figure 4a) via charge delocalization.

This overall 2e- deficiency of the PdO$_4$ moiety suggests that it would be an excellent oxidizer whenever the nearby CeO$_2$ surface is reduced as in CO oxidation via the MvK mechanism. We confirm this by calculating the oxygen vacancy formation energy (OVFE) of O atoms as a function of their distance from Pd. The results, shown in Figure 4c, are compared against the calculated OFVE of the pristine CeO$_2$(100) surface (~102 kJ/mol/O). Intriguingly, while the O atoms in [PdO$_4$] are more difficult to remove (OVFEs of ~133 and ~143 kJ/mol/O) than those of the pristine surface, nearby O atoms are made dramatically more reactive (OVFEs of 22 – 43 kJ/mol). The effect is diminished around a Pd-O distance of ~8 Å (OVFE of 70 kJ/mol) reaching a plateau (of ~88 kJ/mol) at ~12 Å. As a difference in reducibility between 0.1 and 0.2 Pd/nm^2 is seen in our H$_2$-TPR experiments, and our model only allows for a minimum surface density of ~0.19 Pd/nm^2, we suspect a significantly larger distance is required to completely recover pristine surface behavior. Using the average of 8 Å and 12 Å as an approximate "radius of [PdO$_4$] effect", we overlay an illustrative "zone of influence" (semi-transparent blue circles in Figure 4d) around each [PdO$_4$] at different surface Pd densities wherein O atoms are likely activated. Interestingly, areas begin to overlap as surface Pd

density increases, encompassing neighboring [PdO$_4$] by 1.13 Pd/nm^2. This suggests a cumulative effect on oxygen activity as surface Pd density increases.
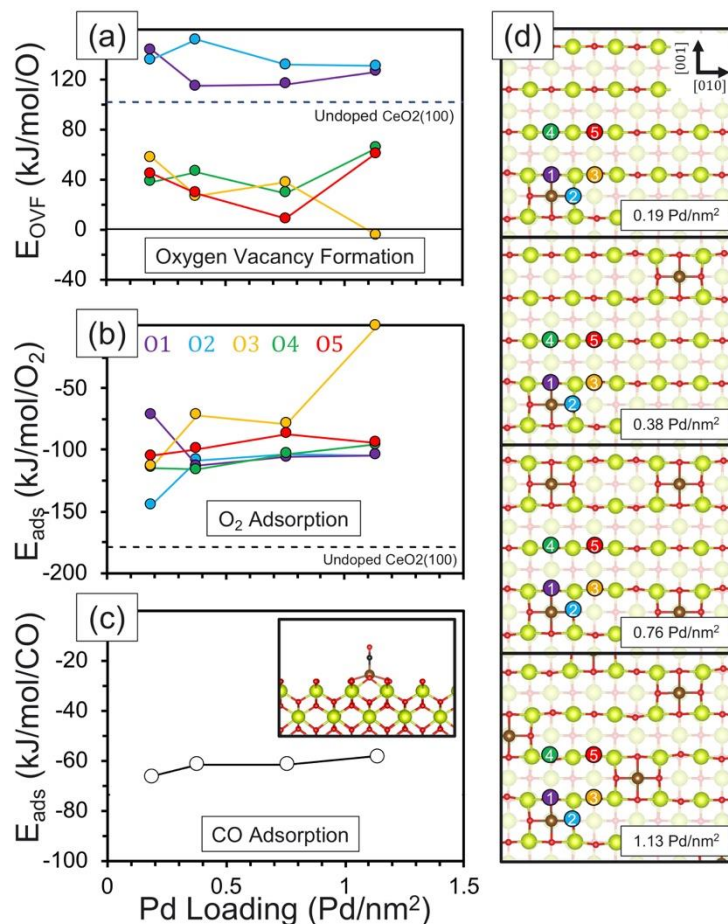

Figure 5. Quantities computed as a function of Pd Loading: (a) oxygen vacancy formation energies, (b) oxygen adsorption energies, and (c) average CO adsorption energies (side view of the corresponding ball-and-stick model is shown inset). (d) Ball-and-stick models of the four surface Pd densities computed here. Symmetrically distinct O atoms are labeled 1 – 5 in each panel of (d). Each series in (a) and (b) corresponds to removal of the labeled O atoms or adsorption of an additional O atom to the labeled O atoms to form a superoxo (O$_2^-$). The series in (c) corresponds to the adsorption of CO on all single Pd atom centers available in each system in (d).

To test this presumption, we compute OVFEs for the five most proximal (out to ~8 Å) O atoms to Pd (including the O atoms in [PdO$_4$]) as a function of surface Pd density, shown in Figure 5a. The results indicate that oxygen activity is progressively enhanced as surface Pd density increases, with a general downward trend in OVFEs seen for the O atoms not directly coordinated to Pd (labeled O3 - O5 in Figure 4). Regardless of surface Pd density, the Pd-coordinated O atoms (labeled O1 and O2 in Figure 4) remain more tightly bound than O atoms in pristine CeO$_2$(100), indicating these O atoms are not likely involved in the CO oxidation reaction. In Figure 5b and 5c, respectively, we show that O$_2$ and CO adsorption energies are

minimally affected by surface Pd density, indicating that the primary cause of the enhanced CO oxidation activity, as seen in experiment, is driven by the increased O reactivity. An analysis of the charge distribution, seen in Figures S16 – S18, reveals that [PdO_4] is consistently reduced after O atom removal, regardless of which O atom is removed. As can be seen in Figure S19, for the O3 atom most proximal to [PdO_4], the most likely participant in CO oxidation, the OVFEs correlate well with the change in work function ($\Delta\Phi$), with large $\Delta\Phi$ corresponding to the highest OVFEs. This indicates that nonlocal electrostatic effects to be the source of the observed OVFE trends.

The OVFE and O_2 adsorption energy of O3 at surface Pd density of 1.13 Pd/nm^2 (see Figure 5a and 5b) deserves highlighting. We find that the OVFE is thermoneutral to within expected errors, suggesting that this O atom should be very active. However, the subsequent re-adsorption of O_2 is lacking an enthalpic driving force so once this O vacancy forms, it will be permanent. This is consistent with experimental results that showed decreased oxygen species adsorption on oxygen vacancies on 4 Pd/CeO_2 (Figure 3). As can be seen in Figure S20, up to 4 such proximal O atoms can be removed, corresponding to two thirds of the available [PdO_4] active sites. This is a significant loss of active O atoms and may explain the experimentally observed loss in specific activity (Figure 1) beyond simple Pd agglomeration.

CONCLUSIONS

Our study highlights a synergy between single Pd atoms on CeO_2 and enhanced catalytic activity, in contrast to the constant-activity behavior typically assumed for single atom catalysts. By combining activity measurements, H_2-TPR, Raman spectroscopy, FTIR, and DFT calculations, we demonstrate that this improvement is due to increased activity of O atoms proximal to Pd, with a surprisingly large area of influence (at minimum 2.0 nm^2) and O activity accumulation as surface Pd density increases. This unique behavior, characteristic of CeO_2 but absent in Al_2O_3, emphasizes the importance of the support.

XANES, EXAFS, DFT and charge analysis allowed us to characterize the Pd/CeO$_2$ active site as an overoxidized square planar [PdO$_4$] complex with Pd in an approximate +2.6 oxidation state and unsaturated valence O atoms in approximately -1.7 oxidation states. The oxidative power of [PdO$_4$] is also shown to have a large lateral range of effect on oxygen activity that accumulates as surface density of [PdO$_4$] increases. This stems from the ability of CeO$_2$ to shuttle charge from oxygen vacancies to the [PdO$_4$] complex, which reduces it to a more stable oxidation state. Both Raman spectroscopy and DFT calculations reveal the limits of this cumulative effect at high surface Pd densities result in overactivation and permanent removal of previously active O atoms. Overall, the most interesting feature is direct correlation of specific activity to CeO$_2$ reducibility rather than Pd. This work invites further investigation into the origin and manifestation of nonlocal effects in single atom catalysts that have hitherto received little attention.

METHODS

Catalysts preparation

The nanocube CeO_2 support, dominated by (100) facets, was hydrothermally synthesized in Teflon-lined stainless steel autoclaves as previous report.[40] Pd/CeO_2 catalysts were prepared by incipient wetness impregnation using $Pd(NH_3)_4(NO_3)_2$ solution followed by calcination at 400 °C for 4 h under air. Pd/Al_2O_3 catalysts were prepared by same method using commercial γ-Al_2O_3 (PURALOX® SBa200, Sasol, SA=200m^2/g). The Pd/Al_2O_3 catalysts were calcined at 700 °C for 1 h using 20% O_2/He (60 ml min^{-1}) as previous report.[23,53] Resulting catalysts were designated as as *X* Pd/CeO_2 and *X* Pd/Al_2O_3 (*X* = surface Pd density, Pd /nm^2)

Catalyst characterization

1. CeO_2 support

XRD pattern of the synthesized CeO_2 was obtained on a D8 Advance (Bruker) using Cu *Kα* radiation ($λ$ = 1.5406 Å) at 40 kV and 40 mA, with a step size of 0.05 in 2$θ$ and a time per step of 0.5 sec in the 2$θ$ range from 10 to 110 °. BET surface area was determined via N_2 adsorption with a BELSORP-max system (Bel Japan) after degas at 150 °C for 4 h. Scanning electron microscopy (SEM) was performed using an SU-8220 (Hitachi). Transmission electron microscopy (TEM) was performed using a JEM-2100 (JEOL).

2. Pd/CeO_2 and Pd/Al_2O_3 catalysts

AC-HAADF-STEM was performed using JEM-2100F (JEOL). XAFS at Pd K-edge (24350 eV) were performed in fluorescence mode at the 7D beamline of the Pohang Accelerator Laboratory (PLS-II). The data was analyzed by the standard method using the *Ab-initio* Feff program.[54]

H_2-TPR experiments were carried out using BELCAT-II (Bel Japan). 0.05 g of Pd/CeO_2 catalysts were pretreated at 400 °C for 30 min under 20% O_2/He flow (60 ml min^{-1}). 0.1 g of Pd/Al_2O_3 catalysts were pretreated at 700 °C for 30 min under 20% O_2/He flow (60 ml min^{-1}). After calcination, the samples were cooled to -80 °C. The thermal conductivity detector (TCD)

signal was stabilized for 2 h and reduction was carried out under a flow of 2% H_2/Ar (60 ml min^{-1}) at a ramp rate of 10 °C min^{-1}. The amount of H_2 consumed was determined from the TCD signal intensities calibrated using pulse of known amount of H_2. 13X molecular sieve was used to remove water produced during the catalyst reduction.

In-situ Raman analysis was performed on WITec alpha300R Micro-imaging Raman Spectrometer equipped with a 532-nm (3.0 mW) Nd-YAG excitation laser and 40× Nikon objective (NA = 0.6). A spectrometer with a grating of 600 gr/nm was used. The Pd/CeO$_2$ catalysts was loaded into a high-temperature reaction chamber (Harrick scientific) and pretreated at 350 °C for 0.5 h under 20% O_2/He (60 ml min^{-1}). The catalysts were cooled to room temperature (RT) and purged with He (60 ml min^{-1}) for 30 min. The catalysts were exposed to 1% CO + 2.5% O_2 /He and 2.5% O_2/He (60 ml min^{-1}) for 5 min in each condition at selected temperatures (RT, 62 and 125 °C). The spectral acquisition was executed with 20 scans at 3 s/scan using an electrically cooled CCD detector.

In situ transmission FTIR experiments were carried out on selected Pd/CeO$_2$ samples using CO as a probe molecule. The home-built IR cell consists of 2 ¾" stainless steel cube equipped with CaF$_2$ windows, connected to a gas handling manifold and a pumping station. The powder samples were pressed onto a tungsten mesh (>80 % IR transmission) and mounted onto a copper sample holder assembly attached to the Cu heating legs of a ceramic feed through. The sample can be heated resistively, and its temperature is monitored by a K type thermocouple spotwelded to the top center of the W mesh. IR spectra were collected with Bruker Vertex 70 spectrometer equipped with a liquid nitrogen-cooled MCT detector. All the spectra were collected at 4 cm^{-1} resolution and each spectrum was the average of 256 scans. The samples were first oxidized at 673 K in ~ 1Torr of O_2 for 1 h, cooled to 295 K in O_2 before evacuating the cell. After evacuation (<5x10^{-8} Torr) a background spectrum was collected with the sample in the IR beam followed by sequential CO introduction into the cell. After equilibration following each CO aliquot an IR spectrum was collected. The highest equilibrium CO pressure in the IR cell ~0.4 Torr.

Catalyst performance

CO oxidation reaction tests were performed in a quartz flow reactor using 0.02 g catalysts supported by quartz wool. Prior to reaction test, Pd/CeO_2 and Pd/Al_2O_3 catalysts were pretreated under a flow of 20% O_2/He (total flow rate of 60 ml min^{-1}) for 30 min at 400 °C and for 1 h at 700 °C, respectively. The activity was measured at 75 °C with feed gas of 1% CO and 2.5% O_2 in He (total flow rate of 60 ml min^{-1}). The outlet gases were analyzed by Agilent 7820A gas chromatograph (GC) using HP-PLOT Q column and TCD. For reasonable conversion level (<10%), the catalysts were diluted with an Al_2O_3 (for Pd/CeO_2 catalysts) or quartz (for Pd/Al_2O_3 catalysts) if needed ($m_{cat + diluent}$ = 0.02 g). Specific activity (TOF, s^{-1}) was calculated based on the total Pd loading, assuming 100% dispersion. Conversions from 110 to 120 minutes were averaged to calculate specific activity at steady state. For 0.1, 0.2 and 0.4 Pd/CeO_2 catalysts, the specific activity at steady state was obtained at least 5 different temperatures for linear Arrhenius plots.

DFT calculations

All calculated solutions to the unrestricted (spin polarized) Kohn-Sham equations on all $Pd/CeO_2(100)$ systems were performed using the CP2K quantum chemical and molecular dynamics simulation package (version 6.1).[55] The Perdew-Burke-Ernzerhof (PBE)[56,57] functional was chosen to describe exchange and correlation, while Grimme's D3-type parameterization[58] with a 15 Å cutoff was chosen to provide dispersion corrections. In CP2K, core electrons and nuclei are described using norm-conserving pseudopotentials of the Goedecker-Tetter-Hutter (GTH) type.[59] Valence electrons were described in a Gaussian – plane wave hybrid basis set scheme[60], using double- ζ Gaussian MOLOPT basis sets[61] (for all elements except Ce) along with a plane wave cutoff of 500 Ry. To properly capture the electronics and redox properties of Ce, its recently reported LnPP1 GTH basis set and pseudopotential[62] were adopted. The GGA+U scheme[63] was also utilized with an effective

Hubbard parameter (U-J) of 0.15 Hartrees (~4.08 eV) selected as specified by Lu et al.,[62] corresponding to LnPP1. Further computational details can be found in the SI.

Data availability

The data that support the findings of this study are available from the corresponding author on request.

Acknowledgements

Author contributions
J.H.K. conceived and designed the project. Y.K. carried out the catalyst preparation, characterization and reaction tests. S.J.C performed EXAFS and the data analysis. K.K. and J.S. carried out IR. G.C., M.S.L, V-A.G. and R.R. designed and performed the DFT calculations. All the authors contributed critically for understanding the reaction mechanisms and participated in discussions and writing of the paper.

Additional Information

Competing interests

The authors declare no competing interests.

References

1   Yang, X.-F. *et al.* Single-Atom Catalysts: A New Frontier in Heterogeneous Catalysis. *Acc. Chem. Res.* **46**, 1740-1748 (2013).

2   Mitchell, S., Vorobyeva, E. & Pérez-Ramírez, J. The Multifaceted Reactivity of Single-Atom Heterogeneous Catalysts. *Angew. Chem. Int. Ed.* **57**, 15316-15329 (2018).

3   Li, X., Yang, X., Huang, Y., Zhang, T. & Liu, B. Supported Noble-Metal Single Atoms for Heterogeneous Catalysis. *Advan. Mater.* **31**, 1902031 (2019).

4   Cui, X., Li, W., Ryabchuk, P., Junge, K. & Beller, M. Bridging homogeneous and heterogeneous catalysis by heterogeneous single-metal-site catalysts. *Nat. Catal.* **1**, 385-397 (2018).

5   Wang, J., Li, Z., Wu, Y. & Li, Y. Fabrication of Single-Atom Catalysts with Precise Structure and High Metal Loading. *Advan. Mater.* **30**, 1801649 (2018).

6   Wu, J., Xiong, L., Zhao, B., Liu, M. & Huang, L. Densely Populated Single Atom Catalysts. *Small Methods* **4**, 1900540 (2020).

7   Tang, C. *et al.* Coordination Tunes Selectivity: Two-Electron Oxygen Reduction on High-Loading Molybdenum Single-Atom Catalysts. *Angew. Chem. Int. Ed.* **59**, 9171-9176 (2020).

8   Liu, J.-C., Xiao, H. & Li, J. Constructing High-Loading Single-Atom/Cluster Catalysts via an Electrochemical Potential Window Strategy. *J. Am. Chem. Soc.* **142**, 3375-3383 (2020).

9   Li, J. *et al.* Ultrahigh-Loading Zinc Single-Atom Catalyst for Highly Efficient Oxygen Reduction in Both Acidic and Alkaline Media. *Angew. Chem. Int. Ed.* **58**, 7035-7039 (2019).

10   Zhao, L. *et al.* Cascade anchoring strategy for general mass production of high-loading single-atomic metal-nitrogen catalysts. *Nat. Commun.* **10**, 1278 (2019).

11   Kunwar, D. *et al.* Stabilizing High Metal Loadings of Thermally Stable Platinum Single Atoms on an Industrial Catalyst Support. *ACS Catal.* **9**, 3978-3990 (2019).

12   Qiao, B. *et al.* Ultrastable single-atom gold catalysts with strong covalent metal-support interaction (CMSI). *Nano Res.* **8**, 2913-2924 (2015).

13   Yang, M. *et al.* Catalytically active Au-O(OH)$_x$-species stabilized by alkali ions on zeolites and mesoporous oxides. *Science* **346**, 1498-1501 (2014).

14   Qiao, B. *et al.* Single-atom catalysis of CO oxidation using Pt_1/FeO_x. *Nat. Chem.* **3**, 634-641 (2011).

15   Yang, T. *et al.* A Theoretical Investigation on CO Oxidation by Single-Atom Catalysts $M_1/\gamma-Al_2O_3$ (M=Pd, Fe, Co, and Ni). *ChemCatChem* **9**, 1222-1229 (2017).

16   Wang, Y.-G. *et al.* CO Oxidation on Au/TiO_2: Condition-Dependent Active Sites and Mechanistic Pathways. *J. Am. Chem. Soc.* **138**, 10467-10476 (2016).

17   Yuk, S. F. *et al.* Selective acetylene hydrogenation over single metal atoms supported on Fe3O4(001): A first-principle study. *J. Chem. Phys.* **152**, 154703 (2020).

18   Lou, Y. & Liu, J. CO Oxidation on Metal Oxide Supported Single Pt atoms: The Role of the Support. *Ind. Eng. Chem. Res.* **56**, 6916-6925 (2017).

19   Mei, D. *et al.* Unique Role of Anchoring Penta-Coordinated Al^{3+} Sites in the Sintering of $\gamma-Al_2O_3$-Supported Pt Catalysts. *J. Phys. Chem. Lett.* **1**, 2688-2691 (2010).

20   Sarma, B. B. *et al.* Metal-Specific Reactivity in Single-Atom Catalysts: CO Oxidation on 4d and 5d Transition Metals Atomically Dispersed on MgO. *J. Am. Chem. Soc.* **142**, 14890-14902 (2020).

21   Abbet, S., Heiz, U., Häkkinen, H. & Landman, U. CO Oxidation on a Single Pd Atom Supported on Magnesia. *Phys. Rev. Lett.* **86**, 5950-5953 (2001).

22   Zhang, Z. *et al.* Thermally stable single atom $Pt/m-Al_2O_3$ for selective hydrogenation and CO oxidation. *Nat. Commun.* **8**, 16100 (2017).

23   Peterson, E. J. *et al.* Low-temperature carbon monoxide oxidation catalysed by regenerable atomically dispersed palladium on alumina. *Nat. Commun* **5**, 4885 (2014).

24   Venkataswamy, P., Jampaiah, D., Lin, F., Alxneit, I. & Reddy, B. M. Structural properties of alumina supported Ce–Mn solid solutions and their markedly enhanced catalytic activity for CO oxidation. *Appl. Surf. Sci.* **349**, 299-309 (2015).

25   Qiao, B. *et al.* Highly active Au_1/Co_3O_4 single-atom catalyst for CO oxidation at room

temperature. *Chinese J. Catal.* **36**, 1505-1511 (2015).

26   Nie, L. *et al.* Activation of surface lattice oxygen in single-atom Pt/CeO₂ for low-temperature CO oxidation. *Science* **358**, 1419-1423 (2017).

27   Zhang, X. *et al.* A Ti-anchored Ti₂CO₂ monolayer (MXene) as a single-atom catalyst for CO oxidation. *J. Mater. Chem. A* **4**, 4871-4876 (2016).

28   Therrien, A. J. *et al.* An atomic-scale view of single-site Pt catalysis for low-temperature CO oxidation. *Nat. Catal.* **1**, 192-198 (2018).

29   Spezzati, G. *et al.* Atomically Dispersed Pd–O Species on CeO₂(111) as Highly Active Sites for Low-Temperature CO Oxidation. *ACS Catal.* **7**, 6887-6891 (2017).

30   Spezzati, G. *et al.* CO oxidation by Pd supported on CeO₂(100) and CeO₂(111) facets. *Appl. Catal. B* **243**, 36-46 (2018).

31   Boronin, A. *et al.* Investigation of palladium interaction with cerium oxide and its state in catalysts for low-temperature CO oxidation. *Catal. today* **144**, 201-211 (2009).

32   Dessal, C. *et al.* Dynamics of Single Pt Atoms on Alumina during CO Oxidation Monitored by Operando X-ray and Infrared Spectroscopies. *ACS Catal.* **9**, 5752-5759 (2019).

33   Cargnello, M. *et al.* Control of Metal Nanocrystal Size Reveals Metal-Support Interface Role for Ceria Catalysts. *Science* **341**, 771-773 (2013).

34   Jeong, H., Bae, J., Han, J. W. & Lee, H. Promoting Effects of Hydrothermal Treatment on the Activity and Durability of Pd/CeO2 Catalysts for CO Oxidation. *ACS Catal.* **7**, 7097-7105 (2017).

35   Hu, Z. *et al.* Effect of Ceria Crystal Plane on the Physicochemical and Catalytic Properties of Pd/Ceria for CO and Propane Oxidation. *ACS Catal.* **6**, 2265-2279 (2016).

36   Jeong, H. *et al.* Highly durable metal ensemble catalysts with full dispersion for automotive applications beyond single-atom catalysts. *Nat. Catal.* **3**, 368-375 (2020).

37   Liu, X. *et al.* Low-temperature catalytic oxidation of CO over highly active mesoporous Pd/CeO₂–ZrO₂–Al₂O₃ catalyst. *RSC Adv.* **6**, 41181-41188 (2016).

38   Slavinskaya, E. M. *et al.* Metal–support interaction in Pd/CeO₂ model catalysts for CO oxidation: from pulsed laser-ablated nanoparticles to highly active state of the catalyst. *Catal. Sci. Technol.* **6**, 6650-6666 (2016).

39   Lee, A. F., Hackett, S. F. J., Hargreaves, J. S. J. & Wilson, K. On the active site in heterogeneous palladium selox catalysts. *Green Chem.* **8**, 549-555 (2006).

40   Wu, Z., Li, M. & Overbury, S. H. On the structure dependence of CO oxidation over CeO₂ nanocrystals with well-defined surface planes. *J. Catal.* **285**, 61-73 (2012).

41   Liu, J.-X., Su, Y., Filot, I. A. W. & Hensen, E. J. M. A Linear Scaling Relation for CO Oxidation on CeO₂-Supported Pd. *J. Am. Chem. Soc.* **140**, 4580-4587 (2018).

42   Ha, H., Yoon, S., An, K. & Kim, H. Y. Catalytic CO Oxidation over Au Nanoparticles Supported on CeO₂ Nanocrystals: Effect of the Au–CeO₂ Interface. *ACS Catal.* **8**, 11491-11501 (2018).

43   Liu, B. *et al.* Interfacial effects of CeO₂-supported Pd nanorod in catalytic CO oxidation: a theoretical study. *J. Phys. Chem. C* **119**, 12923-12934 (2015).

44   Lohrenscheit, M. & Hess, C. Direct Evidence for the Participation of Oxygen Vacancies in the Oxidation of Carbon Monoxide over Ceria-Supported Gold Catalysts by using Operando Raman Spectroscopy. *ChemCatChem* **8**, 523-526 (2016).

45   Kopelent, R. *et al.* Catalytically Active and Spectator Ce³⁺ in Ceria-Supported Metal Catalysts. *Angew. Chem. Int. Ed.* **54**, 8728-8731 (2015).

46   Sun, X. *et al.* FeOₓ supported single-atom Pd bifunctional catalyst for water gas shift reaction. *AIChE J* **63**, 4022-4031 (2017).

47   Luo, M.-F., Hou, Z.-Y., Yuan, X.-X. & Zheng, X.-M. Characterization study of CeO₂ supported Pd catalyst for low-temperature carbon monoxide oxidation. *Catal. Lett.* **50**, 205-209 (1998).

48   Lin, S., Yang, L., Yang, X. & Zhou, R. Redox properties and metal–support interaction of Pd/Ce₀.₆₇Zr₀.₃₃O₂–Al₂O₃ catalyst for CO, HC and NOₓ elimination. *Appl. Surf. Sci.* **305**, 642-649 (2014).

49   Vedyagin, A. A. *et al.* Characterization of active sites of Pd/Al₂O₃ model catalysts with low Pd content by luminescence, EPR and ethane hydrogenolysis. *Appl. Catal. B* **103**, 397-403 (2011).

50   Wu, Z., Li, M., Howe, J., Meyer, H. M. & Overbury, S. H. Probing Defect Sites on CeO_2 Nanocrystals with Well-Defined Surface Planes by Raman Spectroscopy and O_2 Adsorption. *Langmuir* **26**, 16595-16606 (2010).

51   Filtschew, A., Hofmann, K. & Hess, C. Ceria and Its Defect Structure: New Insights from a Combined Spectroscopic Approach. *J. Phys. Chem. C* **120**, 6694-6703 (2016).

52   Schilling, C., Ganduglia-Pirovano, M. V. & Hess, C. Experimental and Theoretical Study on the Nature of Adsorbed Oxygen Species on Shaped Ceria Nanoparticles. *J. Phys. Chem. Lett.* **9**, 6593-6598 (2018).

53   Narula, C. K., Allard, L. F., Moses-DeBusk, M., Stocks, G. M. & Wu, Z. Single Pd Atoms on θ-Al_2O_3 (010) Surface do not Catalyze NO Oxidation. *Sci. Rep.* **7**, 560 (2017).

54   Rehr, J. J., Albers, R. C. & Zabinsky, S. I. High-order multiple-scattering calculations of x-ray-absorption fine structure. *Phys. Rev. Lett.* **69**, 3397-3400 (1992).

55   Hutter, J., Iannuzzi, M., Schiffmann, F. & VandeVondele, J. cp2k: atomistic simulations of condensed matter systems. *WIREs Comput. Mol. Sci.* **4**, 15-25 (2014).

56   Perdew, J. P., Burke, K. & Ernzerhof, M. Generalized Gradient Approximation Made Simple. *Phys. Rev. Lett.* **77**, 3865-3868 (1996).

57   Perdew, J. P., Burke, K. & Ernzerhof, M. Generalized Gradient Approximation Made Simple. *Phys. Rev. Lett.* **78**, 1396 (1997).

58   Grimme, S. Supramolecular Binding Thermodynamics by Dispersion-Corrected Density Functional Theory. *Chem. Eur. J.* **18**, 9955-9964 (2012).

59   Goedecker, S., Teter, M. & Hutter, J. Separable dual-space Gaussian pseudopotentials. *Phys. Rev. B* **54**, 1703-1710 (1996).

60   VandeVondele, J. *et al.* Quickstep: Fast and accurate density functional calculations using a mixed Gaussian and plane waves approach. *Comput. Phys. Commun.* **167**, 103-128 (2005).

61   VandeVondele, J. & Hutter, J. Gaussian basis sets for accurate calculations on molecular systems in gas and condensed phases. *J. Chem. Phys.* **127**, 114105 (2007).

62   Lu, J.-B. *et al.* Norm-Conserving Pseudopotentials and Basis Sets To Explore Lanthanide Chemistry in Complex Environments. *J. Chem. Theory Comput.* **15**, 5987-5997 (2019).

63   Dudarev, S. L., Botton, G. A., Savrasov, S. Y., Humphreys, C. J. & Sutton, A. P. Electron-energy-loss spectra and the structural stability of nickel oxide: An LSDA+ U study. *Phys. Rev. B* **57**, 1505-1509 (1998).

Supplementary Information

Are All Single Atoms Created Equal? *Surface Density Dependent Catalytic Activity of Single Pd Atoms Supported on Ceria*

Yongseon Kim[1,‖], Greg Collinge[2,3,‖], Mal-Soon Lee[2,3], Konstantin Khivantsev[3], Sung June Cho[4,*], Vassiliki-Alexandra Glezakou[2,3], Roger Rousseau[2,3,*], Janos Szanyi[3,*], Ja Hun Kwak[1,*]

[1] Department of Chemical Engineering, Ulsan National Institute of Science and Technology (UNIST), 50 UNIST-gil, Ulsan 44919, Republic of Korea

[2] Physical and Computational Sciences Directorate and Institute for Integrated Catalysis, Pacific Northwest National Laboratory, Richland, WA 99354, USA

[3] Institute for Integrated Catalysis, Pacific Northwest National Laboratory, Richland, WA 99352 USA

[4] Department of Chemical Engineering, Chonnam National University, 77 Yongbong-ro, Buk-gu, Gwangju 61186, Republic of Korea

Corresponding authors: sjcho@jnu.ac.kr, roger.rousseau@pnnl.gov, janos.szanyi@pnnl.gov, jhkwak@unist.ac.kr
[‖] These authors contributed equally.

Figure S1. XRD pattern of synthesized CeO_2. The CeO_2 displays a fluorite cubic structure.
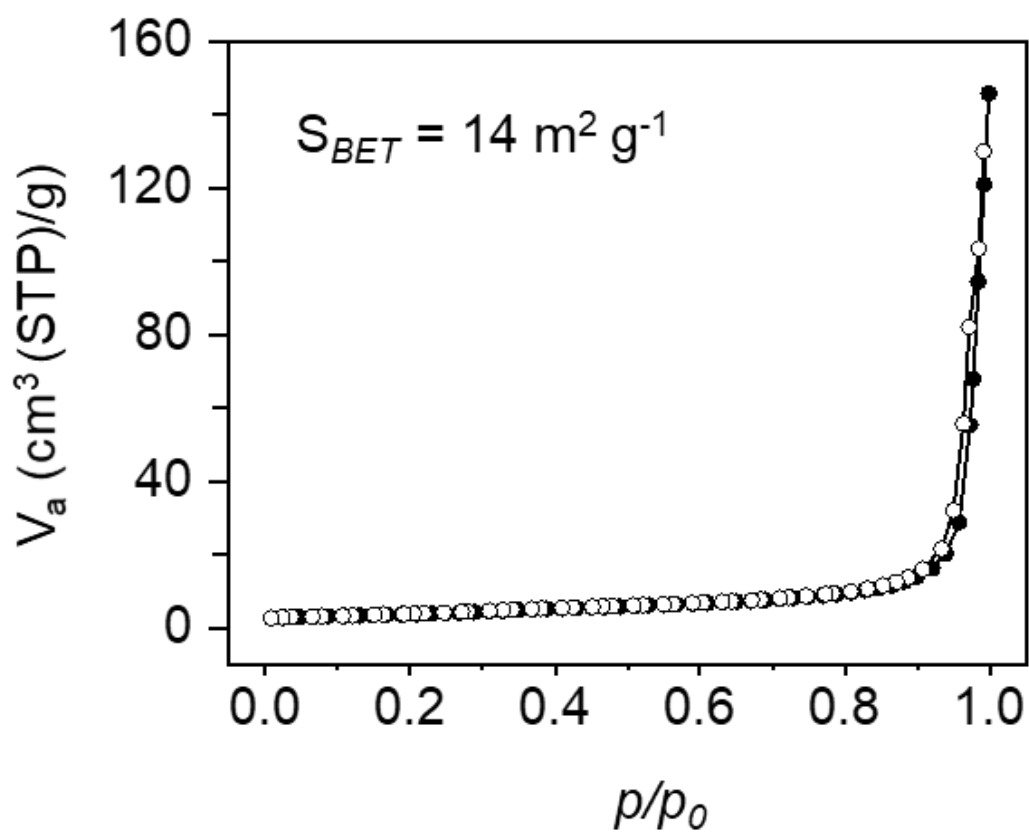
Figure S2. N_2 sorption isotherms for CeO_2 (Closed circle: adsorption, Open circle: desorption). Brunauer-Emmett-Teller (BET) surface area is 14 m^2 g^{-1}.

5
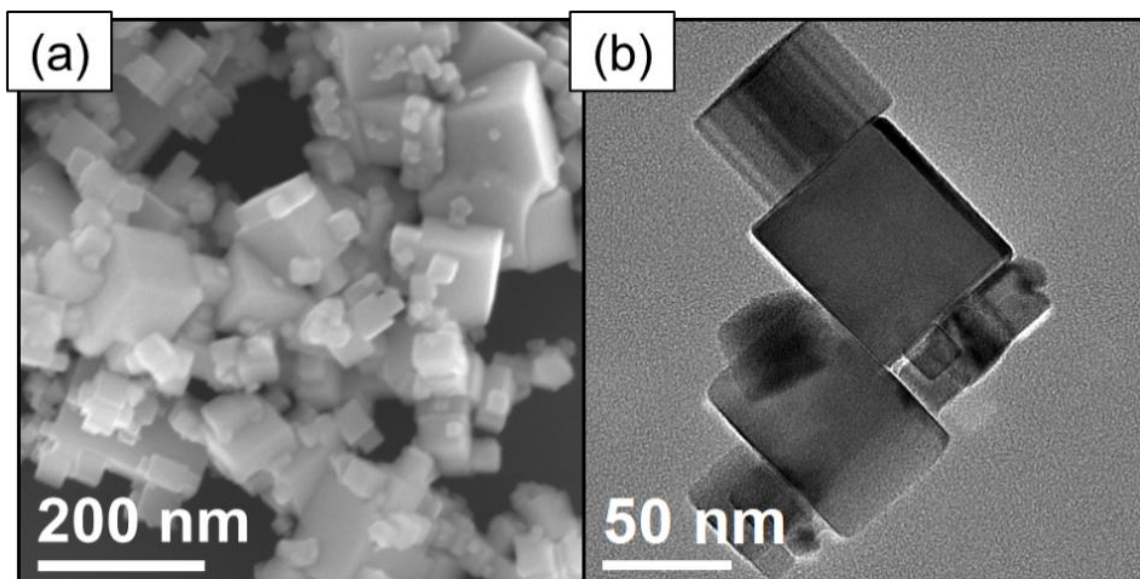
Figure S3. (a) SEM and (b) TEM image of CeO_2. The morphology of CeO_2 nanoparticles is predominantly cube shaped, exposing mostly (100) surface facets.

5
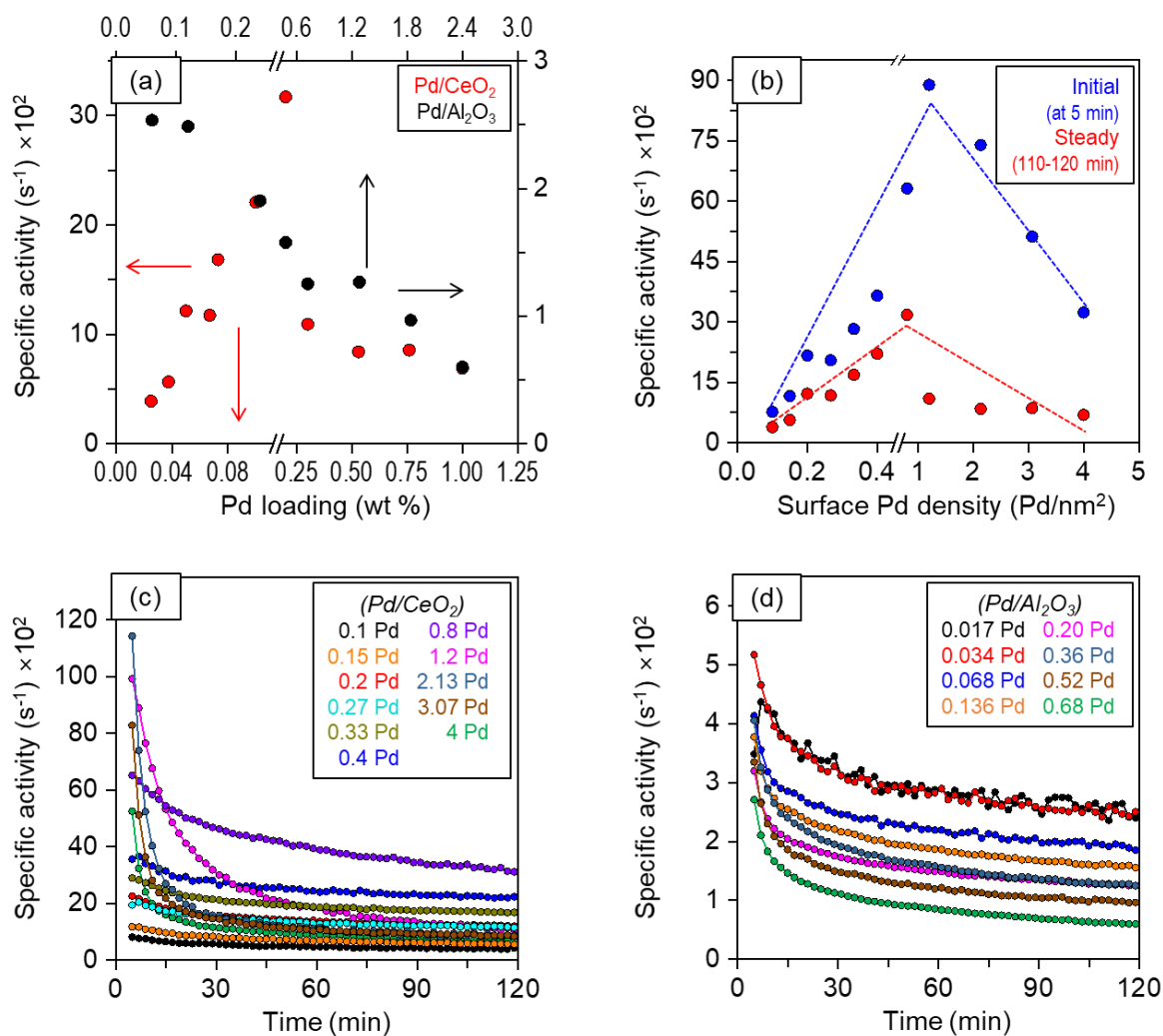
Figure S4. (a) Specific activity of CO oxidation at steady state as a function of Pd loading (%) of Pd/CeO_2 and Pd/Al_2O_3 catalysts, (b) Specific activity of CO oxidation at initial (5 min, blue colored) and steady state (averaged from 110 to 120 min, red colored) as a function of surface Pd density of Pd/CeO_2 (trend lines were manually made by observing the trend of the data points). Specific activity of (c) Pd/CeO_2 and (d) Pd/Al_2O_3 as function of time.
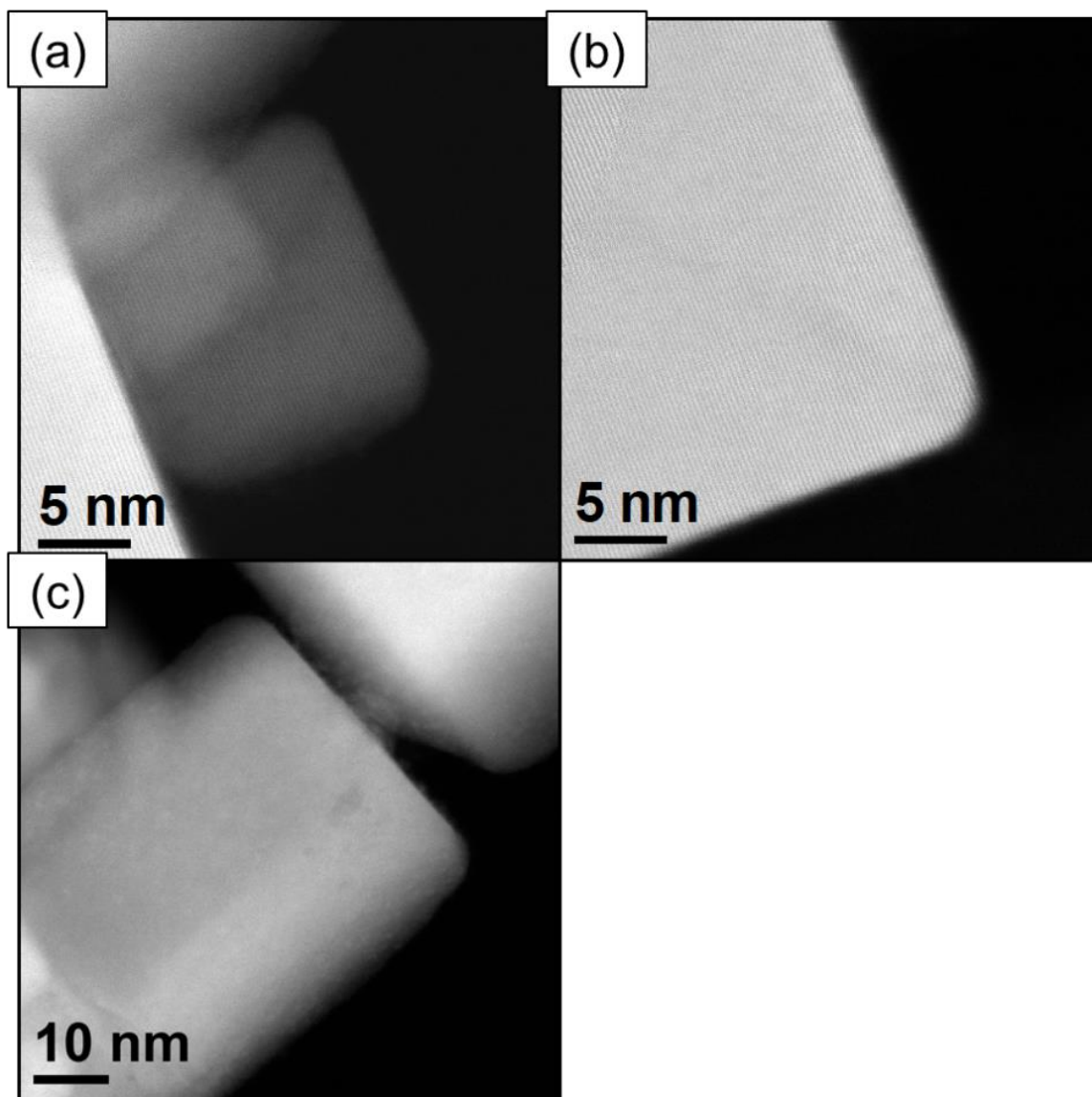
Figure S5. AC-HAADF-STEM images of (a, b) 0.8 Pd/CeO$_2$ and (c) 4 Pd/CeO$_2$.
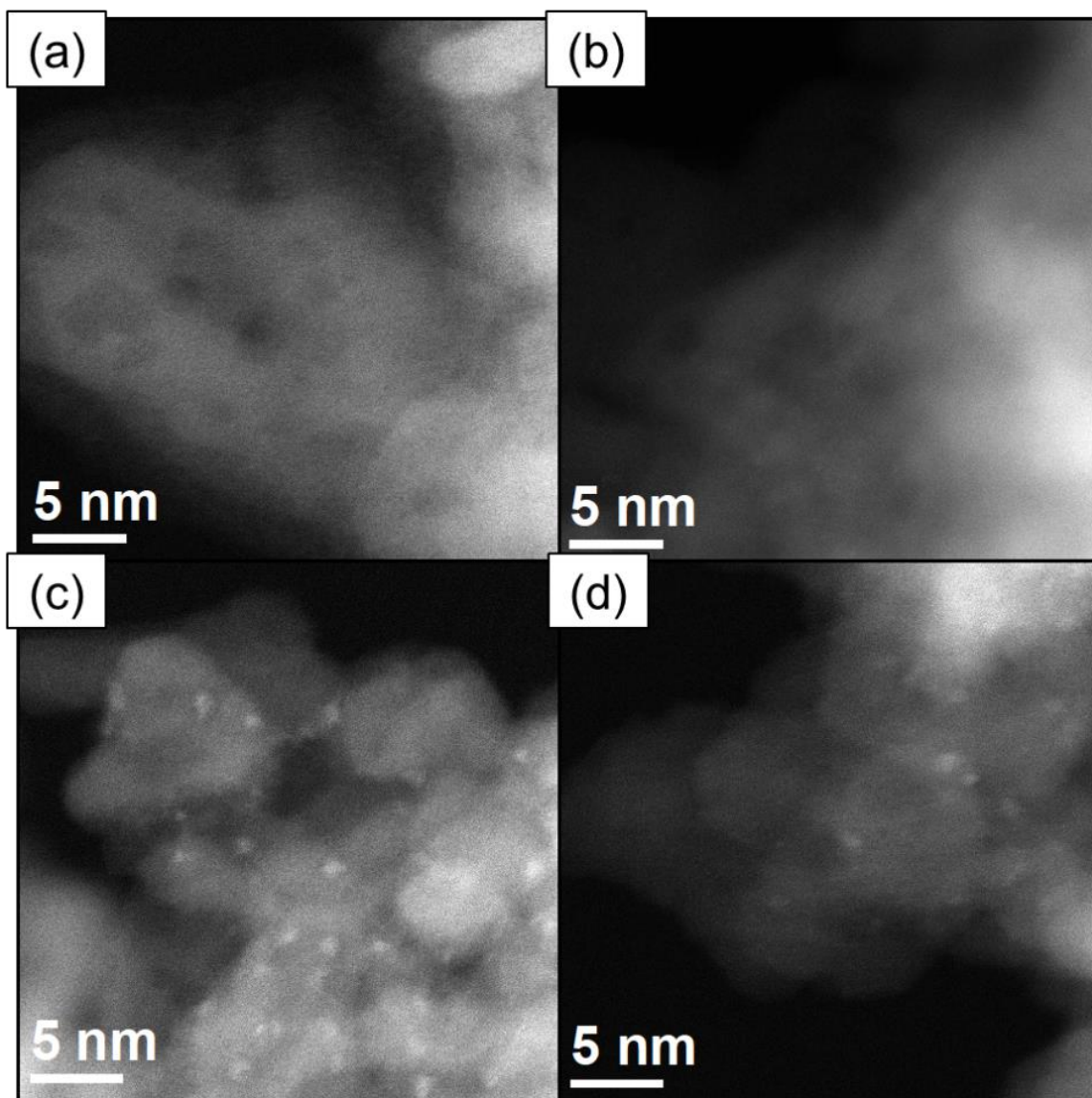
Figure S6. AC-HAADF-STEM images of (a, b) 0.034 Pd/Al$_2$O$_3$ and (c, d) 0.20 Pd/Al$_2$O$_3$.

5
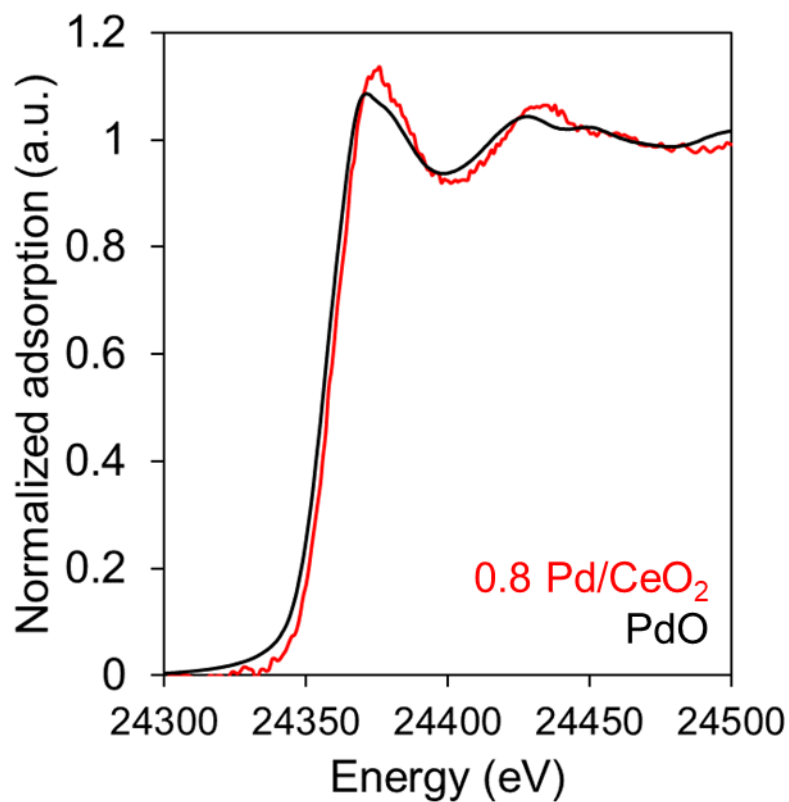
Figure S7. X-ray absorption near edge structure (XANES) spectra of 0.8 Pd/CeO$_2$ and PdO reference.
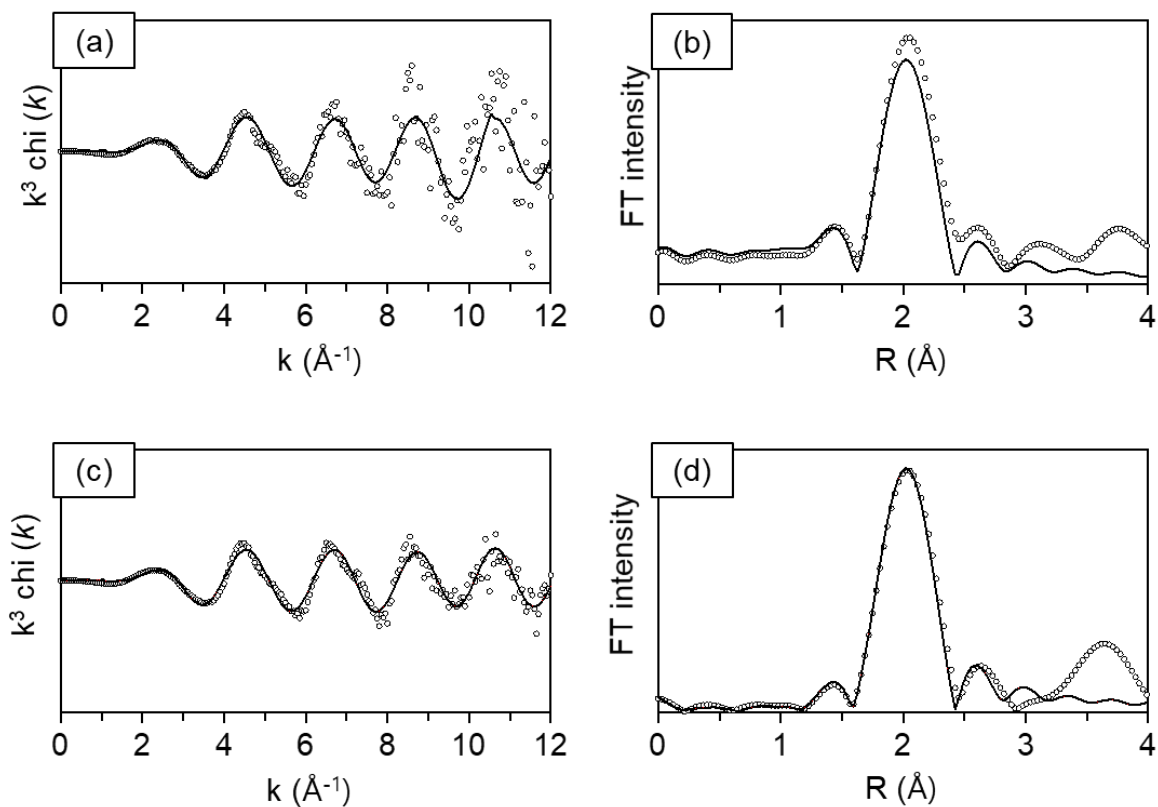
Figure S8. k^3-weighted chi(k) and the corresponding Fourier transform for 0.8 Pd/CeO$_2$ (a, b) and 4 Pd/CeO$_2$ (c, d). The circle and solid line indicate the experimental and fitted spectrum, respectively. The phase shift correction has been made with reference to the Pd-O pair.

5
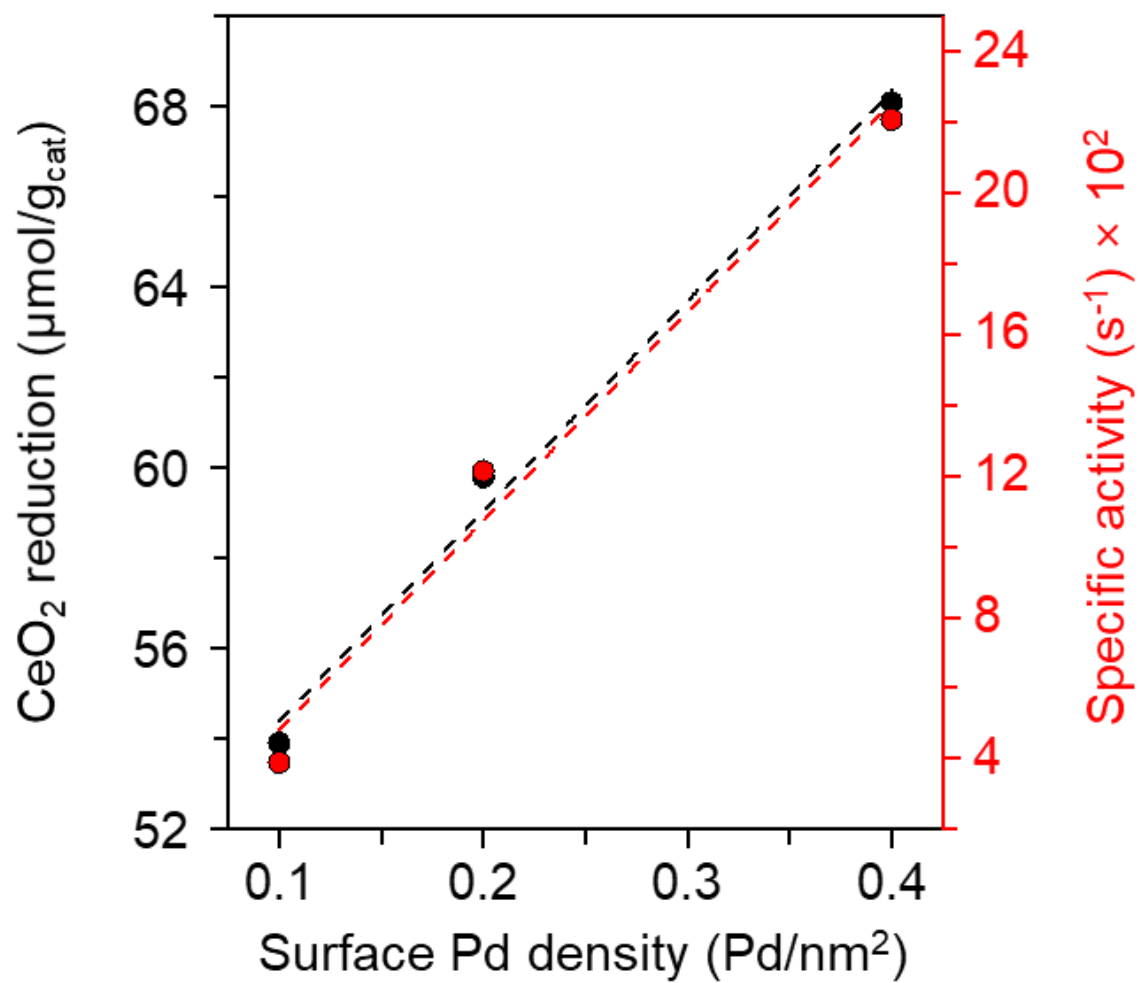
Figure S9. Contribution of CeO$_2$ reduction during H$_2$-TPR and specific activity of Pd/CeO$_2$ as function of surface Pd density.
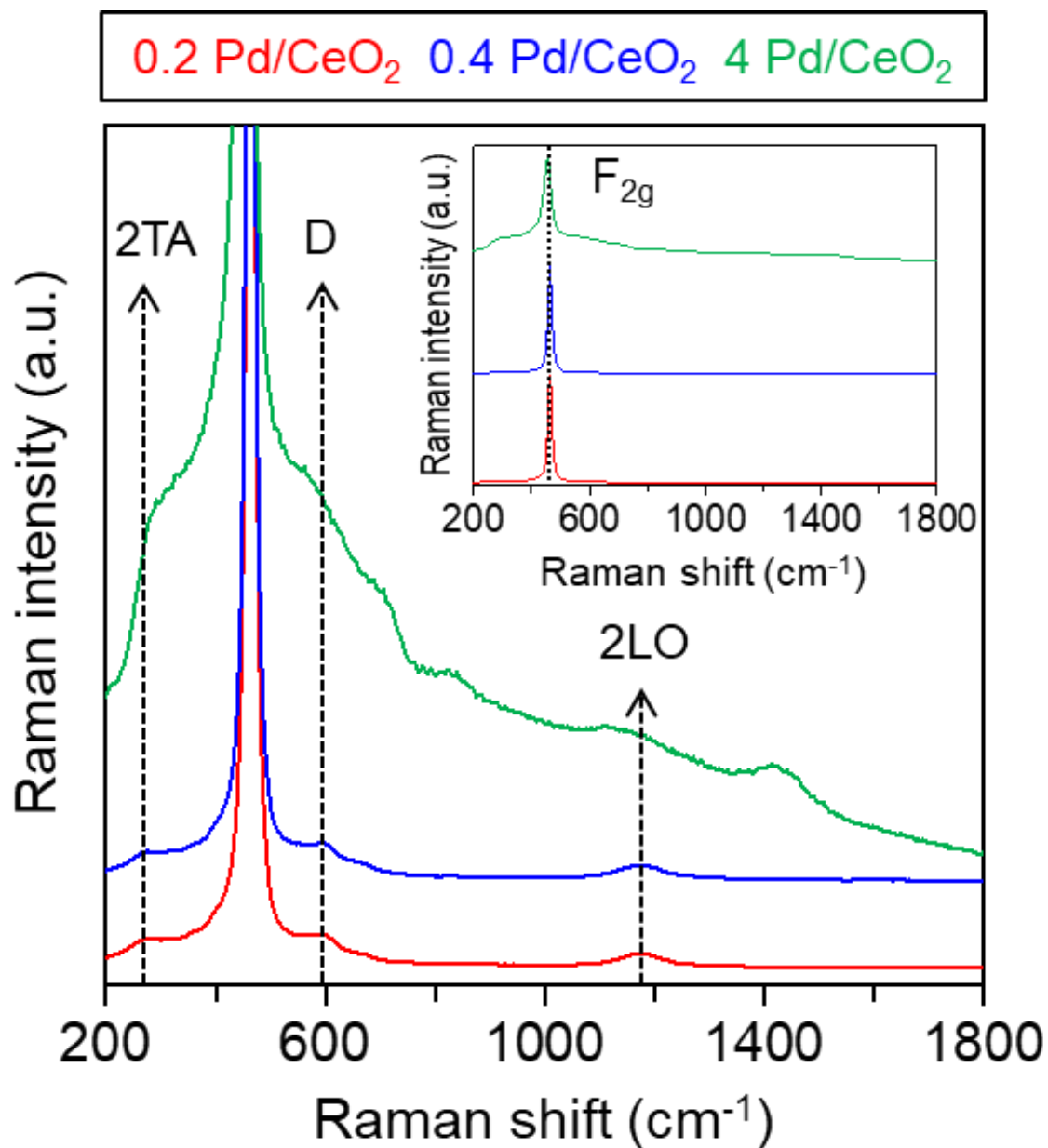
Figure S10. In-situ Raman spectra of 0.2, 0.4 and 4 Pd/CeO$_2$ after pre-treatment. The spectra were obtained at room temperature and under He flow. Raman intensity was normalized with intensity of F$_{2g}$ (450-470 cm^{-1}) band.

5
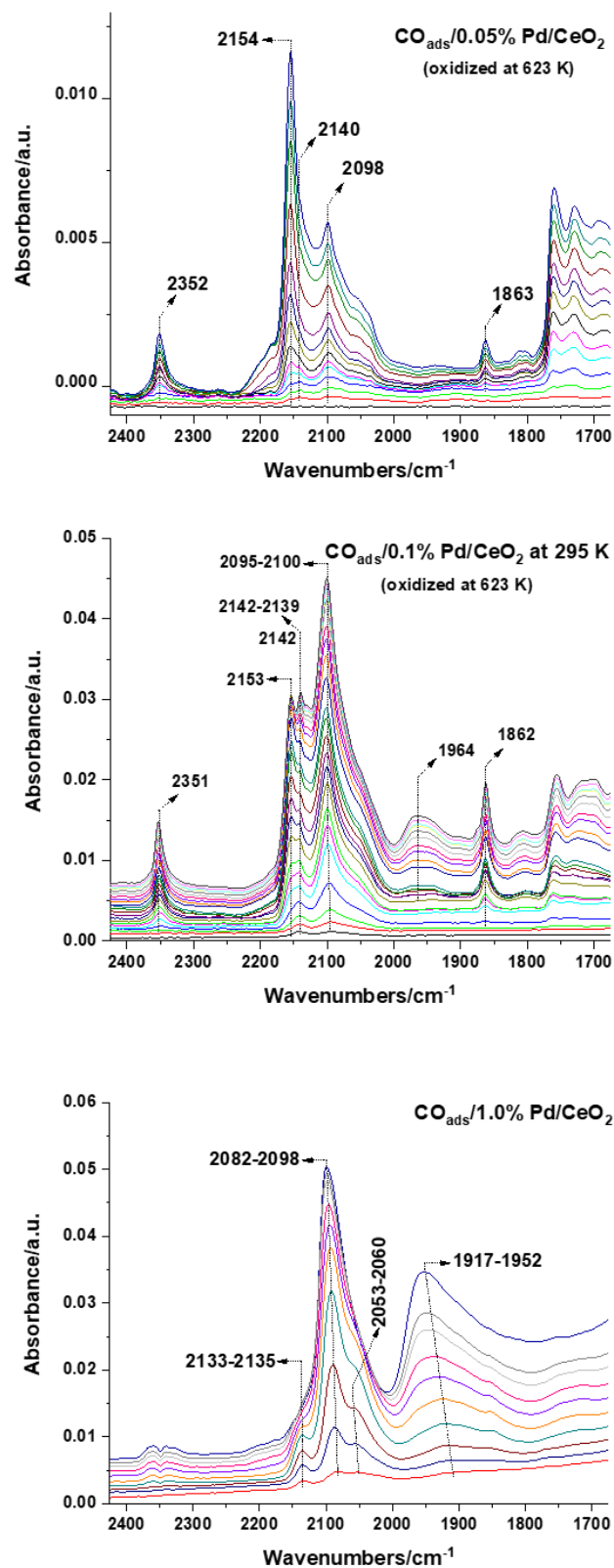
Figure S11. In-situ IR spectra of 0.2, 0.4 and 4 Pd/CeO$_2$. The spectra were obtained during absorbing CO on oxidized catalysts.
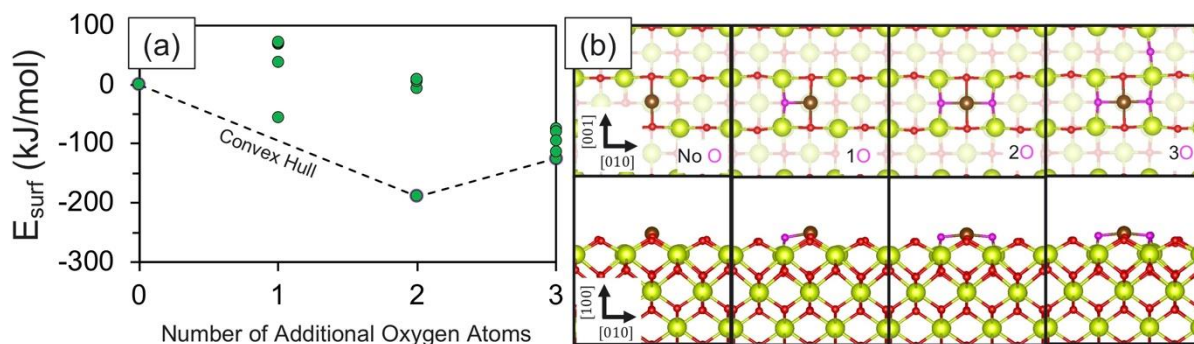
Figure S12. (a) DFT surface energy of the Pd$_1$/CeO2(100) model, seen in the first panel of (b), as a function of the number of additional O atoms adsorbed to the surface at nearby Ce bridge sites. (b) Minimum energy O adsorption configuration for each O atom addition. Green and red atoms are Ce and O of CeO$_2$, respectively; brown and magenta atoms are Pd and O of (PdO$_x$)$_1$.

In Figure S12, we computed the 0 K DFT surface energy defined as:

$$E_{surf}[N_O] = E_{(PdO_x)/CeO_2(100)}[N_O] - E_{Pd/CeO_2(100)}[0] - N_O \left(\frac{1}{2} E_{O_2(g)}\right) \qquad (S1)$$

where $E_{Pd/CeO_2(100)}[N_O]$ is the total DFT energy of the (6×6) Pd/CeO$_2$(100) supercell with N_O additional oxygen adatoms present, and $E_{O_2(g)}$ is the DFT calculated energy of an O$_2$ molecule in the gas phase. The slopes connecting the lowest $E_{surf}[N_O]$ to the lowest $E_{surf}[N_O - 1]$ provides an estimate of the chemical potential to create the structure corresponding to $E_{surf}[N_O]$. To be stable, the states thus connected must have a positive curvature (i.e. constantly increasing slope), which is not the case for any of the points at $E_{surf}[1]$. This results in a very large negative (0 K) chemical potential (~ -95 kJ/mol/O) for the minimum energy structure at $E_{surf}[2]$ with the minimum energy structure at $E_{surf}[3]$ only accessible when the (0 K) chemical potential increases to ~ +63 kJ/mol, a greater than 150 kJ/mol/O difference. Therefore, if a *relatively* modest partial pressure of O$_2$ is applied so as to accomplish *any* O adsorption, which is almost certainly the case during catalyst synthesis, only the (PdO$_2$)$_1$ structure (shown in the third panel of Figure S12b) will be stable. The other structures at $N_O = 2$, where the second O adsorbs in nearby Ce-Ce bridge sites, are too high in energy compared to the minimum energy structure to be stably formed. As noted, a large increase in the applied chemical potential is required to access the minimum energy structure at $E_{surf}[3]$. This strongly suggests that the active sites in Pd/CeO$_2$(100) are (PdO$_2$)$_1$ units, and so this structure was chosen for continued analysis.
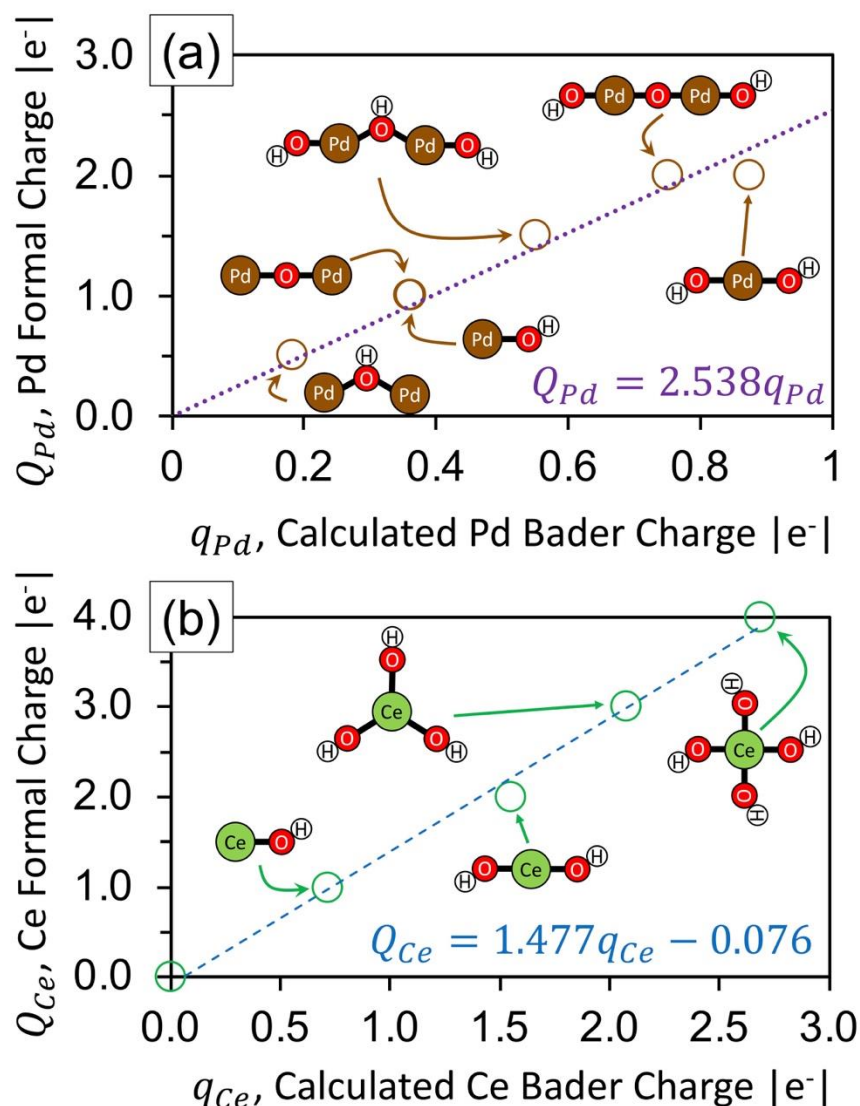
Figure S13. Bader charge calibrations for (a) Pd and (b) Ce. Each data point represents a metal-hydroxide, metal-oxo, or mixed metal oxo/hydroxide complex with a known formal charge. Bader charges were then assessed using the computational methods employed in the rest of the work.

To assess the charge state of the active site, we performed a Bader-partitioning of both the electron and spin density of the $(PdO_2)_1/CeO_2(100)$ system. The electron density Bader charges of Pd and Ce were additionally calibrated against known metal complexes' oxidation states (see Figure S13) to permit the assignment of formal charges. By then comparing, in aggregate, computed formal charges with the spin density Bader charges (see Table S1), we can accurately infer the charge state of each atom in our system. Using this method, we are able to determine Pd to be in an overoxidized >+2 state. This overoxidation occurs due to the presence of the two additional O atoms forming $(PdO_2)_1$. As shown schematically in Figure S13, to balance a Pd^{2+}, these two O atoms (which will become O1 and O2 in Figure 4a of the main text upon adsorption) would need to be O^{1-} radicals, which is a very unfavorable electron configuration. This unfavorability is alleviated, to a degree, by abstracting charge from the two adjacent O atoms of the $CeO_2(100)$ surface (O3 and O4 in Figure 4a of the main text), but this can only bring each O atom (O1 through O4) to a formal -1.5 charge state. To further alleviate their unfavorable electron configurations, the four O atoms, overoxidize Pd past +2—producing a computed +2.58 Pd oxidation state—to achieve

-1.65 O charge states in the final structure. Spin density Bader charges confirm the undersaturation of O atoms as each O atom has a clear non-zero net unpaired electron density (see Table S1). The spin bader charge on Pd is computed to be zero, but visual inspection of the spin density around Pd (Figure 4b of the main text) shows two d-orbital lobes both clearly containing net unpaired electron density but with opposite spins, leading to the overall net zero unpaired charge that we have computed in Table S1. Thus, we have confidence in the assignment of > +2 for Pd based on the Bader partitioning of electron density and Bader calibration curve shown in Figure S13.

Table S1. Summary of calculated excess Bader charge (to the nearest hundredth $|e^-|$) on atoms nearby Pd in the [PdO$_4$] active site as compared to atoms far away. O atom labels refer to those in Figure 4a of the main text.

Atom	Bader Charge (e^-)	Oxidation State (e^-)	Unpaired Bader Charge ($|e^-|$)
Pd	1.02	+2.58	0.00
Surface O of CeO$_2$(100)	-1.12 to -1.13	-2.00[a]	0.00-0.01
O1	**-0.92**	**-1.65**	**0.29**
O2	**-0.92**	**-1.65**	**0.28**
O3	**-0.91**	**-1.65**	**0.34**
O4	**-0.91**	**-1.65**	**0.34**
O5	-1.10	-2.0[a]	0.01
O6	-1.10	-2.0[a]	0.01
O7	-1.10	-2.0[a]	0.01
O8	-1.10	-2.0[a]	0.01
Surface Ce of CeO$_2$(100)	2.32-2.41	3.35-3.44 (4.0[a])	0.00
Ce1	2.41	3.42 (4.0[a])	0.02
Ce2	2.40	3.47 (4.0[a])	0.02
Ce3	2.38	3.49 (4.0[a])	0.02
Ce4	2.37	3.44 (4.0[a])	0.02

[a] Assigned based on charge balance and/or comparison to the bulk CeO$_2$ Bader charges in the same model. Bulk Ce^{4+} have an average Bader charge and average calibrated oxidation state of 2.44±0.02 and 3.52±0.04, respectively.
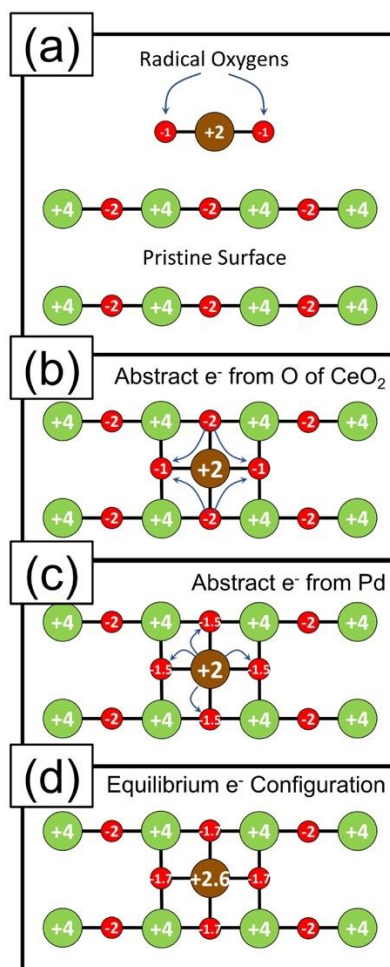
Figure S14. Illustration of how the [PdO$_4$] active site is overoxidized. Brown, green, and red circles represent Pd, Ce, and O atoms, respectively.
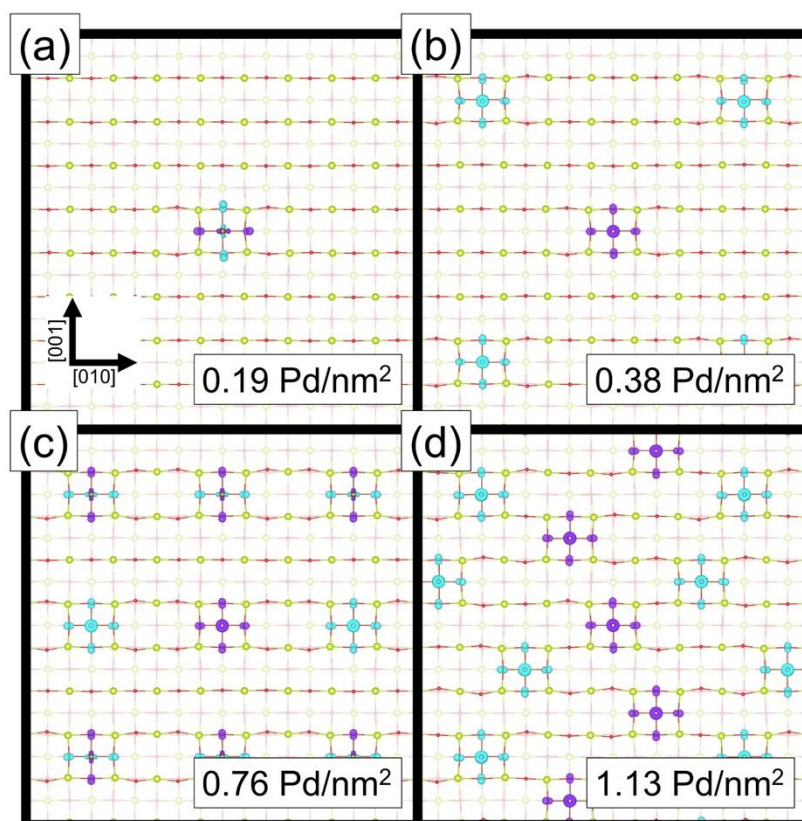
Figure S15. Spin density plots of the $(PdO_2)_1/CeO_2(100)$ system showing the chemical similarity and distribution of active sites in each model constructed to produce surface Pd densities of (a) 0.19, (b) 0.38, (c) 0.76, and (d) 1.13 Pd/nm^2. Spin up and spin down density contours are shown in purple and blue shading, respectively. The relative size of each atom has been reduced to aid the eye, but the color scheme is identical to that used in Figure S12 (isosurface level = 0.04 $|e^-|/Bohr^3$, which is approximately 1/5 the maximum spin density)
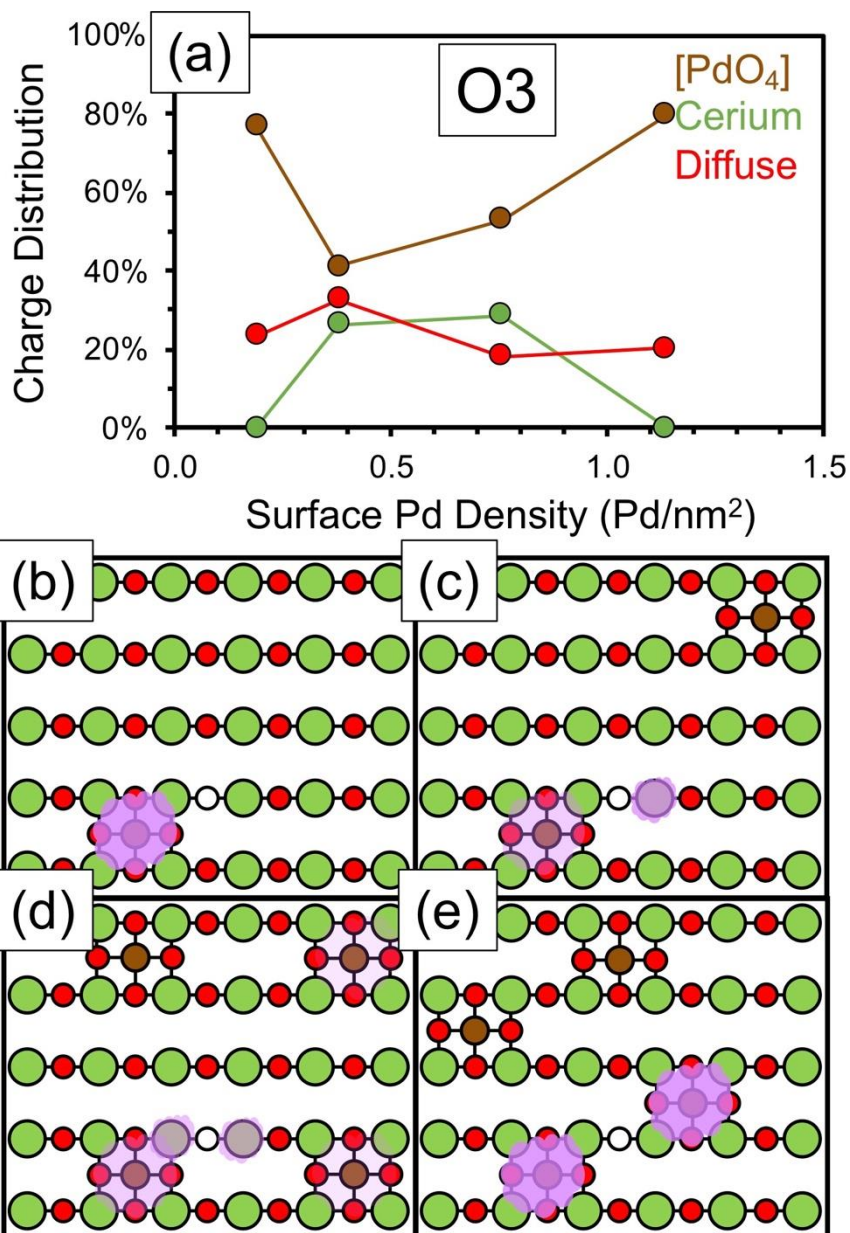
Figure S16. (a) Percent distribution of excess charge left behind after reduction of the O atom occupying O3 site. (b) – (e) A schematic showing where charge was found to be localized (purple clouds; darker purple = more electron density) at surface Pd densities of (b) 0.19 Pd/nm^2, (c) 0.38 Pd/nm^2, (d) 0.76 Pd/nm^2, and (e) 1.13 Pd/nm^2. Brown, green, and red circles represent Pd, Ce, and O atoms, respectively.

5
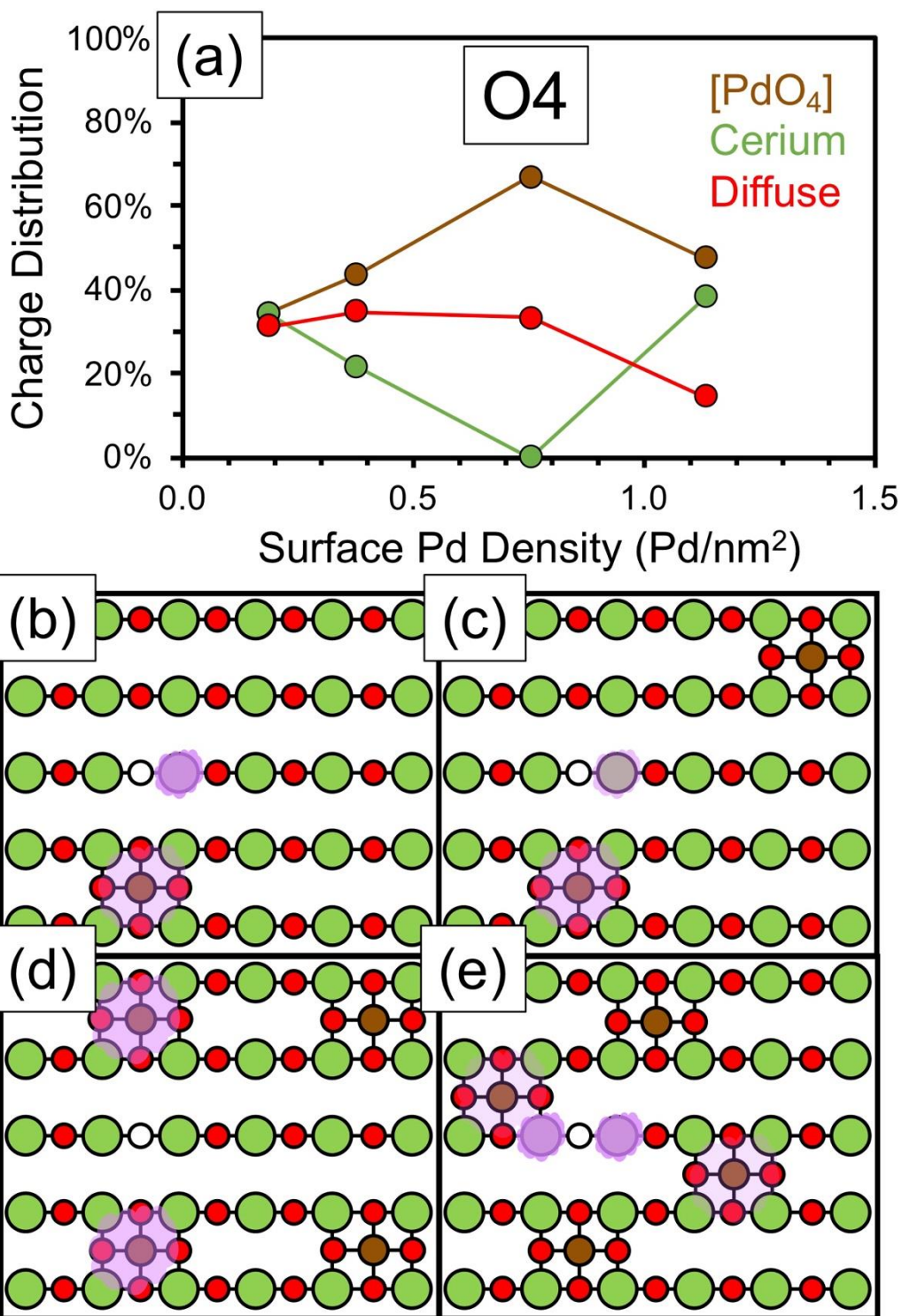
Figure S17. (a) Percent distribution of excess charge left behind after reduction of the O atom occupying O site 4. (b) – (e) A schematic showing where charge was found to be localized (purple clouds; darker purple = more electron density) at surface Pd densities of (b) 0.19 Pd/nm^2, (c) 0.38 Pd/nm^2, (d) 0.76 Pd/nm^2, and (e) 1.13 Pd/nm^2. Brown, green, and red circles represent Pd, Ce, and O atoms, respectively.

5
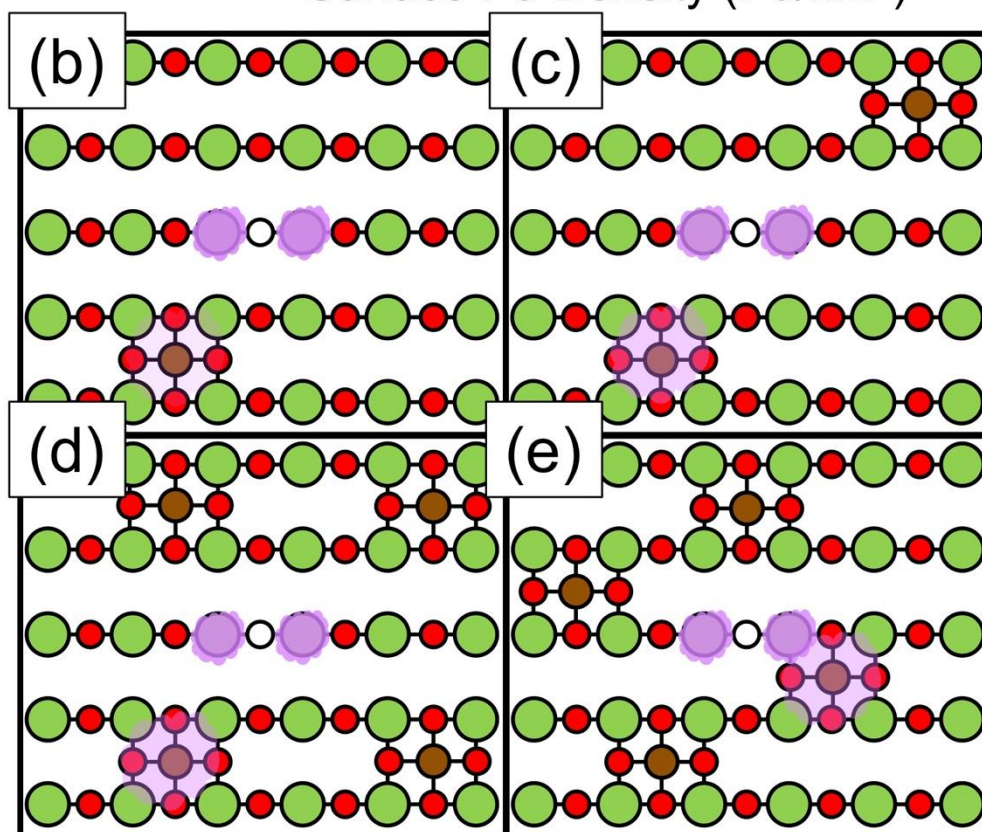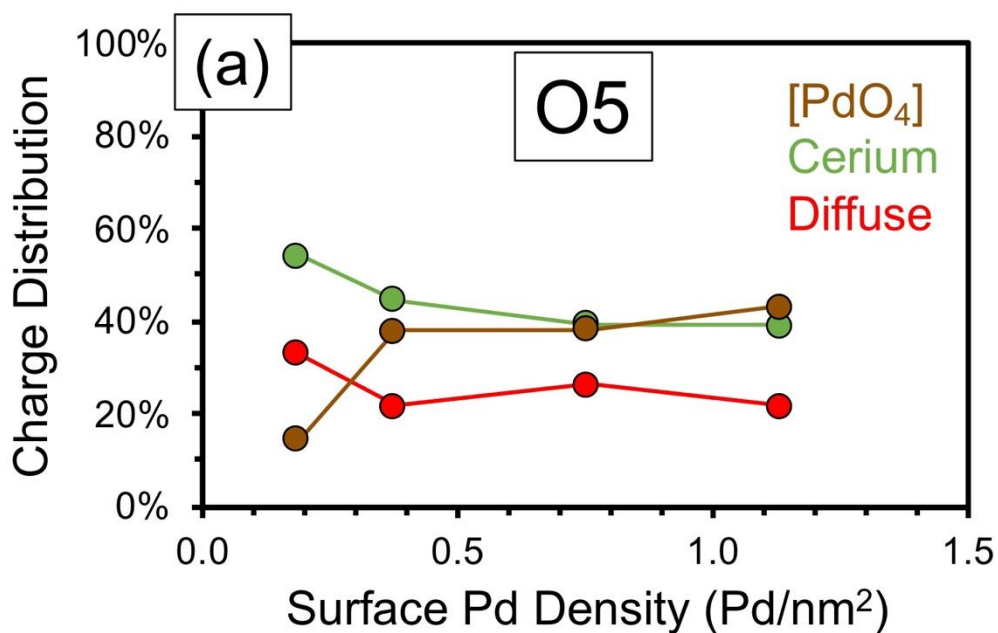
Figure S18. a) Percent distribution of excess charge left behind after reduction of the O atom occupying O site 5. (b) – (e) A schematic showing where charge was found to be localized (purple clouds; darker purple = more electron density) at surface Pd densities of (b) 0.19 Pd/nm^2, (c) 0.38 Pd/nm^2, (d) 0.76 Pd/nm^2, and (e) 1.13 Pd/nm^2. Brown, green, and red circles represent Pd, Ce, and O atoms, respectively.

5
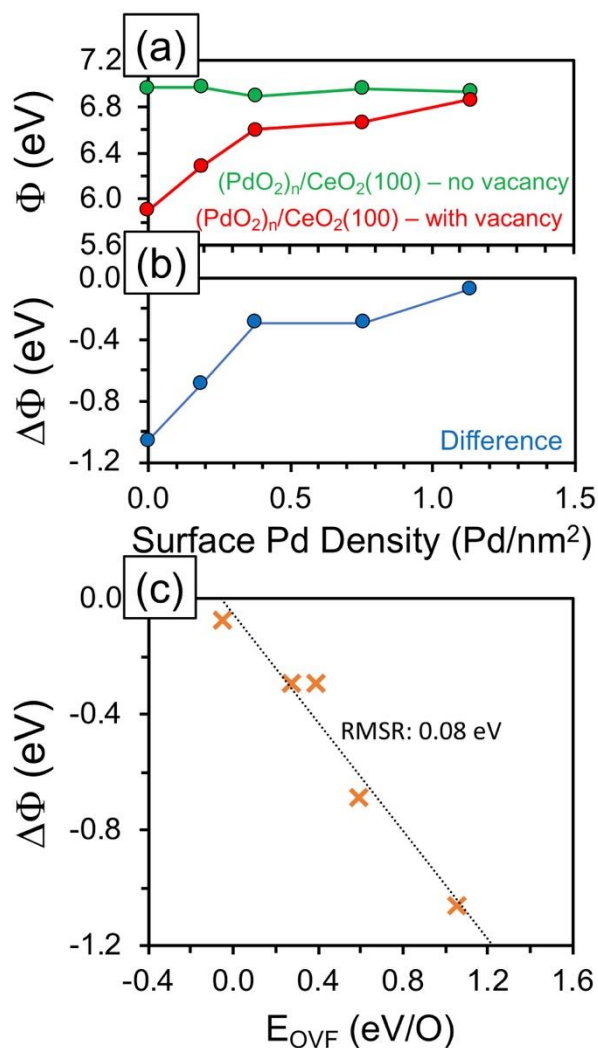
Figure S19. (a) Computed work functions (Φ) for the Pd-doped $CeO_2(100)$ surface with (red line) and without (green line) O vacancies as a function of surface Pd density. Here, the O atom labeled O3 in Figure 5 of the main text was removed to form the O vacancy. (b) Work function change ($\Delta\Phi$) as a result of forming this O vacancy. (c) Work function change plotted against the corresponding OFVE, showing excellent correlation between the two quantities. Note that the OVFE has been plotted in units of eV/O to more closely match the units of the work function.
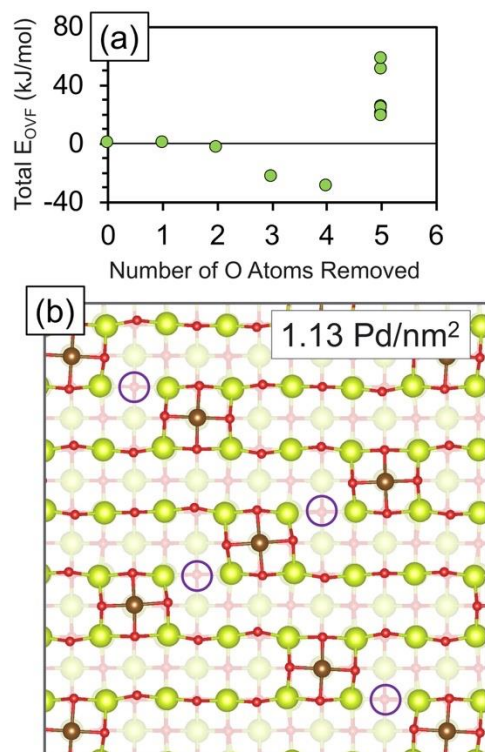
Figure S20. (a) total OVFE (extensive property) as a function of the number of O atoms removed from the 1.13 Pd/nm² model. (b) 1.13 Pd/nm² model after exothermic removal of 4 O total O atoms. Color scheme is identical to that used in Figure S12.

In Figure S20, we computed the total OVFE as:

$$E_{OVF,tot}[N_O] = E_{total}[N_O] - E_{total}[0] + N_O \left(\frac{1}{2} E_{O_2(g)} \right) \tag{S2}$$

where $E_{total}[N_O]$ is the total DFT energy of the (6×6) Pd/CeO$_2$(100) supercell wherein N_O oxygen atoms have been removed, and $E_{O_2(g)}$ is the DFT calculated energy of an O$_2$ molecule in the gas phase.